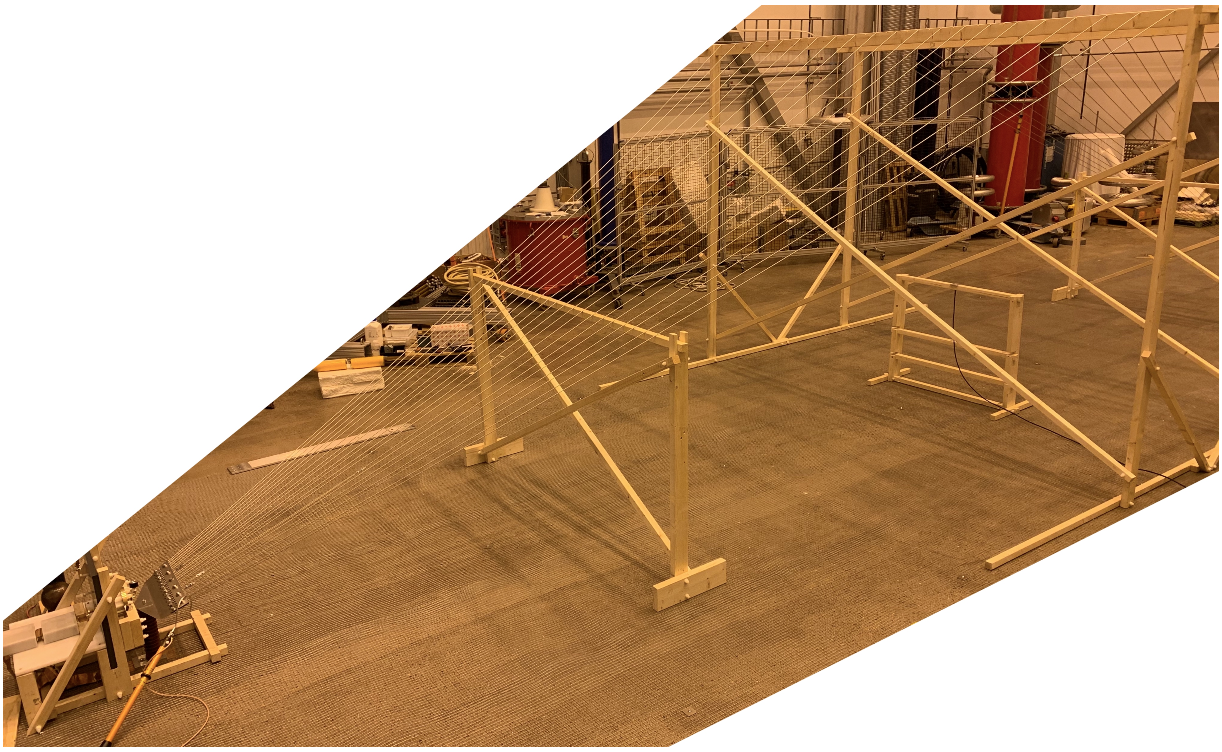

Development of prototype testbed for EMP radiated susceptibility testing

Aiming for compliance to test standard MIL-STD-461G RS105

Master's thesis in Electric Power Engineering

DANIEL ÅKERBERG

DEPARTMENT OF ELECTRICAL ENGINEERING
DIVISION OF ELECTRIC POWER ENGINEERING

CHALMERS UNIVERSITY OF TECHNOLOGY
Gothenburg, Sweden 2021
www.chalmers.se

Master's thesis 2021

Development of prototype testbed for EMP radiated susceptibility testing

Aiming for compliance to test standard MIL-STD-461G RS105

DANIEL ÅKERBERG

CHALMERS
UNIVERSITY OF TECHNOLOGY

Department of Electrical Engineering
Division of Electric Power Engineering
Chalmers University of Technology
Gothenburg, Sweden 2021

Development of prototype testbed for EMP radiated susceptibility testing
Aiming for compliance to test standard MIL-STD-461G RS105
DANIEL ÅKERBERG

Supervisor: Joni Klüss, RISE High Voltage unit
Examiner: Yuriy Serdyuk, Department of Electrical Engineering

Master's Thesis 2021
Department of Electrical engineering
Division of Electric power engineering
Chalmers University of Technology
SE-412 96 Gothenburg
Telephone +46 31 772 1000

Cover: EMP testbed setup with the EMP generator to the left and the radiating transmission line to the right.

Gothenburg, Sweden 2021

Development of prototype testbed for EMP radiated susceptibility testing
Aiming for compliance to test standard MIL-STD-461G RS105
DANIEL ÅKERBERG
Department of Electrical Engineering
Division of Electric Power Engineering
Chalmers University of Technology

Abstract

In the modern society, complex electronic devices are widely used that, either intentionally or unintentionally, radiate signals imposing a risk of interferences with other electronics. To meet a growing urge for uninterrupted operation of electronic devices and systems, testing for approving sufficient electromagnetic compatibility are essential. Such tests, including radiated susceptibility tests, are described in the globally used military test standard MIL-STD-461G. This project aimed to develop a testbed for radiated susceptibility testing for objects sized up to 1x1x1 m3. The test procedure comprises generation of a high voltage pulse and injection of the pulse into a radiation system for creating a transverse electromagnetic field to which the test object is exposed. For the test to be valid, the electromagnetic pulse should provide the front time of maximum 2.3 ns, full width at half maximum within 18-28 ns and the electric field amplitude of minimum 50 kV/m.

The testbed materiel produced within this project includes a radiation system constituted by a 3 m high transmission line composed by 21 conducting wires arranged in a parallel plate resembling structure, a water resistor to make a matched termination of the transmission line, a pressure vessel including a pulse trigger spark gap and field derivative sensors for measuring both electric displacement field and magnetic flux density. FEM based simulations were performed to verify design parameters of the transmission line and the spark gap.

In the experiments, a low inductance, 200 kV rated capacitor bank of 4 nF was charged with a voltage impulse of 900 ns front time originating from a Marx generator. Further, electromagnetic pulses were generated by rapidly discharging the capacitor bank into the transmission line via the pulse trigger spark gap enclosed in the vessel filled with SF6 gas at pressure up to 3 bar. Prominent scattering in the trigger voltage was observed, which probably was caused by impurities in the gas system. Electromagnetic pulses with the front time of 8 ns were successfully generated. The pulse amplitude of 173 kV was obtained, but only occasionally due to issues with external flashovers in the pulse generator. The amplitude of reliably repeatable pulses was 132 kV. Consequently, the electric field requirement of minimum 50 kV/m was not fully fulfilled that was shown by the compilation of the results from the electric field simulations and measured signal attenuation in the transmission line.

The analysis of the results suggests the ways for further improvements. Thus, it is found that the testbed premises (the high voltage laboratory with grounded walls, floor and ceiling) implicated undesired waves reflections, which need to be damped. Further, an evaluation of different measurement cables emphasized the need of using properly shielded cables to suppress noise level. Various types of transmission line termination resistors were tested and it was concluded that a water resistor was preferred as it features low inductance and its resistance value could easily be adjusted to make a properly matched termination. In addition, the used field sensors would need to be calibrated to give

absolute values of the electric field amplitude.

Keywords: Electromagnetic pulse, EMP, EMP generator, EMP simulator, EMP testbed, Electromagnetic interference, Electromagnetic compability, EMC, Radiated susceptibility testing, MIL-STD-461G RS105.

Acknowledgements

First and foremost I want to thank my supervisor Joni Klüss for always being available for discussions and encouragement throughout this project. Your experience was a key factor helping to realise this project and your endless source of positive energy has been truly inspiring. Furthermore, I want to express my gratitude to my examiner Yuriy Serdyuk for pleasant guidance in this project and during several courses in the master's programme as well. I also want to give a heartfelt thank to Tatu Nieminen for all support with technical challenges related to configuring and operating various setups in the high voltage laboratory. In the construction phase, Tomas Persson and his colleagues at RISE mechanical workshop contributed with high quality service and materiel. Also, I want to thank Abd Zahed for valuable input to discussion of design aspects of radiating systems. Finally I want to thank RISE, the high voltage unit in specific, for the opportunity to perform this thesis project and the confidence I was given.

Daniel Åkerberg, Borås, June 2021

Contents

List of Figures

List of Tables

Acronyms

AC	Alternating current
ASEA	Allmänna Svenska Elektriska Aktiebolaget
B-dot	Derivative of magnetic flux density
CW generator	Cockcroft-Walton generator
D-dot	Derivative of electric displacement field
DC	Direct current
EM	Electromagnetic
EMC	Electromagnetic compability
EMI	Electromagnetic interference
EMP	Electromagnetic pulse
EUT	Equipment under test
FEM	Finite element method
FFT	Fast fourier transform
FWHM	Full width at half maximum
GA	General Atomics
GTEM cell	Gigahertz transverse electromagnetic cell
HEMP	High altitude electromagnetic pulse
HF	High frequency
HV	High voltage
LI	Lightning impulse
PEC	Perfect electric conductor
PMC	Perfect magnetic conductor
RF	Radio frequency
RFI	Radio frequency interference
RISE	Research Institutes of Sweden
RS	Radiated susceptibility
S-parameter	Scattering parameter
SF6	Sulphur hexaflouride
SI	Switching impulse
TEM	Transverse electromagnetic

1 Introduction

Electronic devices and electric control systems are central in everyday life in the modern society. Applications ranges from telecommunication, monitoring, industry processes, medical care equipment, autonomous vehicles, power stations etc. Electronic devices could malfunction temporarily or break permanently. Depending on application, malfunction of certain electronic devices might lead to severe consequences such as harm to humans or hardware and loss of income or important data. Thus, providing continuous operation of electronic devices and control systems is critical in many applications. Electromagnetic (EM) radiation constitute a risk of causing unwanted downtime in electric systems. When exposed to an externally originating electric or magnetic field, electronic devices may partly or completely malfunction. This phenomena is known as electromagnetic interference (EMI). The considered frequency range of such electromagnetic waves are typically up to 1 GHz, for higher frequencies interference can also occur, but is in that case denoted as Radio Frequency interference (RFI) [1]. The term electromagnetic compability (EMC) defines the research field of electronic devices functionality during exposure of EM fields, i.e. its resistance to EMI.

There are different sources of EM fields. Some sources are natural, e.g. thunderstorms, solar storms and electrostatic discharges. There are also man-made sources which could be either intentional or unintentional. Any active electric device emit some EM signals as an unwanted side effect. Examples of sources of unintentional EM fields are devices with switching circuits, i.e. inverters, where the switching moment may give voltage ripple leading to voltage peaks and oscillation of high frequency signals. There are regulations for maximum allowed values of unintentional EM emission for commercial electronic devices. Examples of intentional EM sources are jammers that interferes with wireless communication systems. Furthermore, there are and high power weapon-generated transient electromagnetic pulses (EMP) that could both interfere with and possibly cause permanent damage to electric devices. Examples of such weapons are nuclear bombs for which a detonation naturally is succeeded by an EMP and specially designed EMP weapons which are a type of directed-energy weapon. The latter mentioned weapon type could be accessible for both civilians and military where electronic warfare is a possible application. [1].

Thus, it could be desirable to design electronic equipment so that it can withstand exposure of EMP in a proper way without malfunction. Testing and verifying sufficient immunity and robustness towards EMP is important when designing critical electric equipment. Some product end users could demand that the device of interest have successfully passed tests of EMC that prove sufficient immunity to EMI.

Research institutes of Sweden (RISE) is an independent research institute operating in various research areas. RISE have multiple types of testbeds for testing, measuring, certifying and calibrating. The High Voltage (HV) unit together with the EMC unit at RISE have experienced a growing demand of performing EMP tests from their customers, with a specific request for a test standard named ”RS105” from *MIL-STD-461G* that addresses radiated susceptibility (RS). Testbeds for RS testing are commonly referred to as EMP simulators or high altitude EMP (HEMP) simulators. In order to perform RS tests, improved and extended test equipment is needed to make a new testbed in the HV laboratory at RISE [2]. The main need includes an EMP generator capable of generating fast voltage impulses, a transmission line (TL) that carries the EMP and radiates an EM field and a system measuring the generated pulse and the electric field.

1.1 EMC test standards

There are various types of global test standards used for EMC where military EMC test standards play a major role. The present military standard *MIL-STD-461G* has been issued by the United States Department of Defence and have come to be used even outside US military [3]. Among many different type of test standards, ”RS105” is included in *MIL-STD-461G*. To mention other similar existing EMC test standards, there is a swedish standard *SS-EN 61000-4-25/A2* from SEK Svensk Elstandard [4]. This standard is actually an amendment, in this case basically a translation, of the original version *IEC 61000-4-25* from International Electrotechnical Commission. Naturally however, the military test standard MIL-STD-461G RS105 is of main interest in this project as this is requested from RISE and their customers. In *MIL-STD-461G*, four main types of electromagnetic interference EMI are specified; Radiated emission, Conducted emission, Radiated susceptibility, and Conducted susceptibility [5]. For radiated emission, the interfering signals originate from the equipment under test (EUT) and are radiated to the surroundings via air. For conducted emission the interfering signals originates from EUT and are conducted via cables to measurement systems. For radiated susceptibility the EUT is exposed to radiated EMI originating from external source. For conducted susceptibility the EUT is exposed to EMI from an external source via cables making galvanic contact to the test object. Included in the test standard, for each of these four types of EMC tests, are several subcategories that defines various test procedures further. ”RS105” is one of the test procedures included in the radiated susceptibility test category.

1.1.1 Military test standard for radiated susceptibility

The specific test standard *MIL-STD-461G RS105* defines the requirements for radiated susceptibility with transient electromagnetic fields. Some highlights from ”RS105” are

- A transverse electromagnetic (TEM) wave should be applied.
- Radiation system type should be either TEM cell, parallel plate transmission line or equivalent.
- Minimum five pulses are required, maximum rate is one pulse per minute. Pulse rise time in the range from 1.8 ns to 2.8 ns. Pulse full width at half maximum (FWHM) within 23 ns ± 5 ns.
- Peak value of electric field, $\hat{E}$, is required to be within the range 50 kV/m $\leq \hat{E} \leq$ 100 kV/m. The electric field should be measured at five specified locations using D-dot or B-dot field derivative sensors which are further described in Section 2.2.3.
- The usable test volume, e.g. the maximum size of EUT, is determined by size of radiation system. If the radiation systems the height above ground plane, width and length are denoted h, w and l respectively, the size of EUT must not exceed a height of $h/3$, width of $w/2$ nor length of $l/2$.

- Top plate of radiation system should preferably be distanced from closest surrounding metallic object at a distance of at least two times the plate height above ground.

A clarification of the denoted geometrical dimensions of the radiation system is shown in Figure 1.1 where all variables represents a distance except of α that is an angle. The length of interest when determining usable test volume is here denoted as l_1. The denoted orientation of the cartesian coordinate system with unit vectors x, y and z in the figure is used throughout this report.

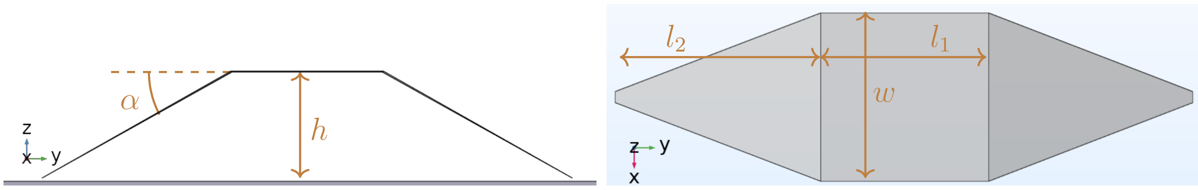

(a) Side view (yz-plane). (b) Top view (xy-plane).

Figure 1.1: Sketch of radiation system including dimension parameters.

The required standard test pulse can be described as a double exponential function, see (2.1). The shape of the standard test pulse is visualised in both time domain and frequency domain (using a one sided FFT) in Figure 1.2.

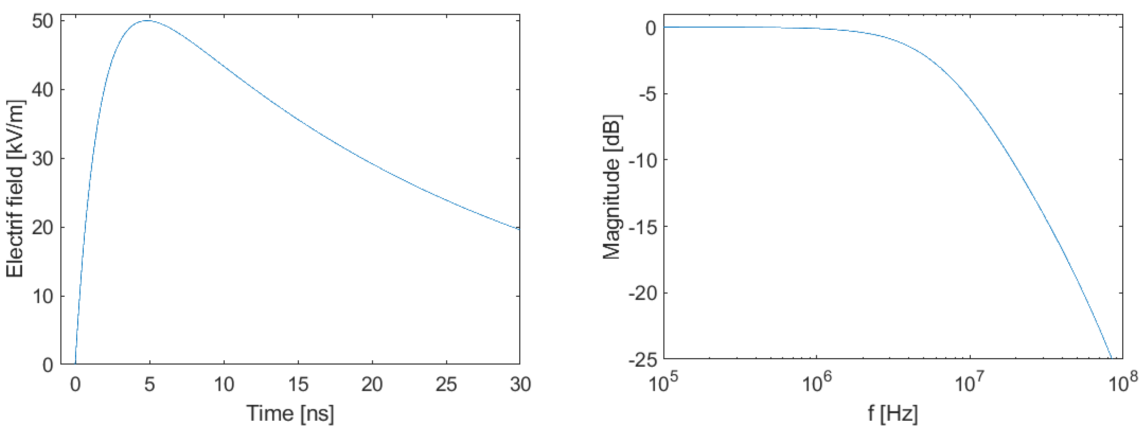

(a) Pulse displayed in time domain. (b) Pulse displayed in frequency domain.

Figure 1.2: Standard test pulse specified by *MIL-STD-461G RS105.* [5].

The "RS105" test standard also specifies needed measurement systems as

- HV probe of minimum 1 GHz bandwidth to be placed at beginning of radiation system.
- Field derivative sensor (D-dot or B-dot probe) with an appurtenant integrator with a time constant of 10 times the overall pulse width.
- Storage oscilloscope of minimum single shot bandwidth of 700 MHz and sampling rate of minimum 1 GS/s. The oscilloscope should be placed in a shielded enclosure and read signal from both HV probe and field derivative sensor.

For the full list of requirements stated by the test standard, see [5].

1.2 Project aim

The objective is to design and construct a complete testbed for military EMC testing according to test standard *MIL-STD-461G RS105* for test objects sized up to 1x1x1 m^3. The testbed should include an EMP generator consisting of a HV impulse generator with an associated radiation system. Its intended area of use is to expose, in testing purpose, electronic equipment to EMPs which need to be repeatable and formed with a magnitude and shape according to present military test standard ”RS105”.

1.3 Problem description

A complete prototype of an EMP testbed should be designed and constructed. To meet the objectives of this project the following sub-problems needs to be processed.

- EMPs are of high power and can therefore not be directly supplied from the grid, a solution for intermediate pulse energy storage is required. This energy system must be handled properly in terms of charging and discharging.
- Repeatably for succeeding EMPs generated in testbed and avoid interference from charging circuit and surroundings.
- Design of a pulse shaping circuit to achieve a magnitude, duration and shape (rise-time and FWHM) of the EMP as specified in *MIL-STD-461G RS105*.
- All parts and components in the testbed needs to have sufficient ability to handle electric stress. A design aspect could be to mitigate the magnitude of the electric field at critical points to avoid flashovers.
- Suppress eventual disturbance or performance deteroriations from stray capacitance and stray inductance.
- An EMP trigger system consisting of a spark gap or other alternative switch for emitting EMPs. The EMP testbed needs to be controlled and monitored at sufficient safety distance.
- Proper impedance matching should be ensured where needed in the radiation system in order to suppress voltage wave reflections as those could possibly damage the EMP generator if leading to voltage levels exceeding rated levels.
- Measure the electric field intensity in the EMP testbed. Measure the EMP waveform at the EMP generator output.
- Time-effective and tractable assemble and disassemble of the EMP testbed.
- The EMP generator should have an output voltage of variable magnitude in order to vary height of radiation system and still generate the same electric field amplitude in the test volume.

1.4 Scope

The output waveform of the EMP generator should be customised according to present test standard. The EMP generator will not be designed for emitting pulses of any other, arbitrary, waveform.

Possible options of different types and configurations for temporary storage of EMP energy in the EMP generator circuit are not reviewed as two rapid discharge capacitors dedicated for this purpose already had been bought by RISE in advance of this project work.

Different charging mechanisms of the rapid discharge capacitors and EMP trigger options are over-viewed in the literature pre-study in the Chapter 2, however not all were tested experimentally because some custom laboratory equipment, such as a suitable DC generator, was not in possession of RISE HV unit.

The EMP testbed is planned to be stationary and used in laboratory environment only. It should be designed for test-objects of limited size of 1x1x1 m^3, these dimensions were chosen based requests from customers of RISE.

The EMP testbed itself should only be used by RISE to perform test services for customers. Economical aspects are not be considered, i.e. the profitability from eventual income-generating assignment the EMP generator could provide to RISE is not evaluated as this is done by managers at RISE.

An investigation of the interference and material damage EMP:s could cause to electronic equipment is not performed. No test-objects are analysed in this project as the EMP generator and radiation system themselves are the primary objects to validate. Performing actual test services for customers is beyond the scope of this project.

2
Theory

In this chapter, relevant theory of impulse voltage generators, propagation of electromagnetic waves and transmission lines used as radiating antennas are presented. The basic principle of operation of impulse voltage generators is described and its parts presented with emphasis on the spark gap. General equations for electromagnetic waves are introduced and how these apply on transmission lines including phenomenon as characteristic impedance and reflection/transmission coefficient. Lastly, different radiation system geometries are presented and compared.

2.1 Impulse voltage generator

Impulse voltage generators are used in HV laboratories to create impulse voltages for testing purpose and simulation of overvoltage. In contrast to HV AC and DC generators with capability of providing continuous voltage supply, an impulse generator provides voltage impulses of short duration for analysing transient phenomenon. Impulse voltages are characterised by peak voltage, front time or rise time and FWHM. Front time and rise time are two slightly different ways of characterising the pulse front. Front time is defined as the duration in which the voltage rise from 0 % to 100 % of peak value while rise time is the duration of voltage rise from 10 % to 90 %. Hence the same pulse will have a rise time that differs from its front time but both ones describe the pulse front in an appropriate way. There are various test standards that require specific impulse characteristics, two common standard test pulses in high voltage application are standard lightning impulse (LI) and standard switching impulse (SI). In the test standard "RS105" an allowed range for the rise time and FWHM is specified, see Section 1.1.1. The "RS 105" standard test pulse has significantly faster rise time and FWHM compared to standard LI and SI pulses. The electric field, E(t), to be generated in an "RS105" test can be expressed by a double exponential function.

$$E(t) = E_0(e^{-\frac{t}{\tau_2}} - e^{-\frac{t}{\tau_1}}) \tag{2.1}$$

where E_0 is an amplitude scaling factor, t is time, e is the base of the natural logarithm, τ_1 and τ_2 are time constants. Typical values for a "RS105" standard test pulse are E_0= 65 kV/m, τ_2 = 25 ns and τ_1 = 1.67 ns and is plotted in Figure 1.2.

Analytic conversion between front and tail time constants to rise time and FWHM is non-trivial but some suggested conversions have been suggested in [6]. Even though a simple conversion from rise time to front time is lacking, it is natural that the front time is slightly larger than the rise time and this can be used as an approximation. Selection of circuit components in an impulse generator can be done with help of desired time constant of double exponential expression, using (2.2), (2.4) and (2.5), thus the given values of τ_2 and τ_1 can be used when designing an impulse generator.

To generate impulse voltages, a capacitive impulse generator circuit can be used.

Due to limitation of maximum output voltage of a single stage impulse generator, i.e. voltage rating of the capacitors, it is common to use a multi stage generator, also called Marx-generator, where the output of several stages are connected in series to achieve higher output voltages. A simplified electric circuit model of a multi stage generator modelled as an equivalent single stage impulse generator is shown in Figure 2.1, where R represent physical resistors, G represents a spark gap, C_D is the energy storing discharge capacitor and C_L is the load capacitance including the capacitance of the test object and any parallel mounted device such as measurement equipment like HV dividers and denoted pulse shaping capacitor if used.

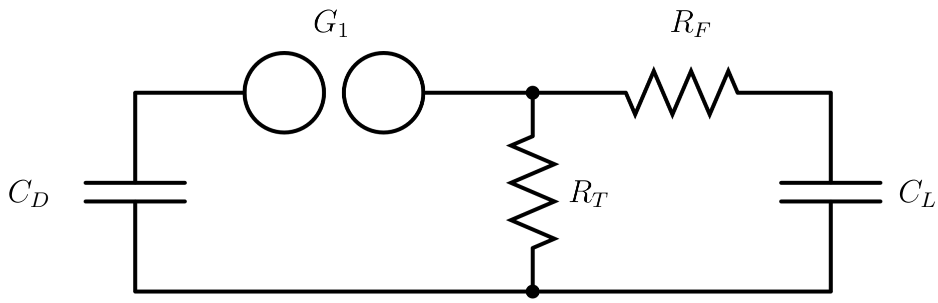

Figure 2.1: Simplified single stage equivalent electric circuit of a multi stage impulse generator.

The principle of operation of an impulse generator is that a storage capacitor, C_D, is pre-charged by an external source to a voltage level V_0. A spark gap, G_1, is used as a switch which is normally open. When the electric field stress in the gap exceeds the dielectric strength of the gap, a conductive channel is formed as the gap breaks down and the switch is now conducting as the spark gap has ignited. It remains conducting as long as the electric field stress in the gap is above the threshold level of extinguishing. With G_1 conducting, C_D is discharged via R_F and the stored energy is used to charge C_L that experiences a impulse voltage which can be described as a double exponential time dependent function

$$v(t) = V_0 \eta \frac{\tau_2}{\tau_2 - \tau_1}(e^{-\frac{t}{\tau_2}} - e^{-\frac{t}{\tau_1}}) \tag{2.2}$$

where V_0 is the initial voltage level across C_D, τ_1 is the pulse front time constant, τ_2 is the pulse tail time constant and η is the voltage efficiency given by

$$\eta = \frac{\hat{v}}{V_0} = \frac{C_D}{C_D + C_L} \tag{2.3}$$

where $\hat{v}$ is the peak voltage experienced by the load. The front time constant is given by

$$\tau_1 = R_F \frac{C_D C_L}{C_D + C_L} \tag{2.4}$$

and the tail time constant is given by

$$\tau_2 = R_T(C_D + C_L) \tag{2.5}$$

and are valid for the circuit configuration presented in Figure 2.1 [7].

The advantages of a spark gap as switch/trigger system is that the trigger voltage is easily controlled and that the conducting channel in the spark gap automatically extinguishes when the voltage stress over the spark gap is reduced and becomes insulating once again. A spark gap typically consist of two metal spheres of diameter, D, separated with a gap distance d_{gap}. The ratio $\frac{D}{d_{gap}}$ has to be sufficiently large to ensure satisfying level of homogeneity of the electric field in the gap. This is important in order to get good accuracy in the voltage breakdown level, V_{bd}, which in this application is the desired voltage for the spark gap to become conducting. Tabulated values of the relation between V_{bd} and the product of pressure p and distance d_{gap} can be used and is further described in Section 2.1.2 [7]. As electric breakdowns include stochastic events the given values for V_{bd} refers to the voltage level entailed with 50 % probability of breakdown.

All electric circuit or loop have a self-inductance which value depends on physical size and geometry and permeability of surrounding medium. Naturally the electric circuit of an impulse generator have some inherent stray inductance. As can be derived from Amperes' Law, larger dimensions of a current loop yields larger magnetic flux linkage which result in greater inductance [8]. Hence, keeping dimensions and current loops as small sized as possible is a key design factor for reducing inductance. The simple relation

$$v(t) = L\frac{di(t)}{dt} \tag{2.6}$$

where t is time, v is voltage, L is inductance and i is current describes hos inductance prevents instantaneous change in current magnitude. A high stray inductance in an impulse generator slows down rise time of the generated pulse. Hence, a low inductance of the generator is essential for creating an EMP with short front time.

A multi stage HV impulse generator typically has a large physical size to ensure sufficient clearances to avoid discharges and therefore suffers a high stray inductance that can not be neglected. For the testbed, ambient conditions applies meaning the surrounding dielectric media is air. To minimise risk of unwanted discharges, clearances between energised and grounded parts must be sufficiently large. This design criteria is contradictory to keeping inductance low in terms of physical size of the generator. Guidelines of required minimum clearances for ambient air condition can be found in IEC standard. For a standard LI impulse with rod-structured electrode the minimum clearance is 320 mm for a pulse amplitude of 170 kV and 380 mm for a pulse amplitude of 200 kV [9].

By introducing insulation liquids or solids the effective dielectric strength can be increased compared to having a path from HV electrode to ground through air only. The reason is that insulation liquids and solids typically have high dielectric strength yielding high breakdown voltages. A typical insulation liquid is mineral oil and typical solid insulation materials are paper, polymer and glass [7].

2.1.1 Model of rapid discharge circuit for EMP generator

To enable pulses of faster rise time than standard LI impulses, a secondary generator circuit that is designed for low inductance and rapid discharge can be used. A circuit diagram for an impulse generator and a rapid discharge circuit is shown in Figure 2.2. The left part highlighted in green represents a Marx multistage impulse generator, the middle part highlighted in blue represents the rapid discharge circuit and the part to the right highlighted in red represents the TL. Consequently, the multi stage impulse generator is not used to generate an EMP pulse but rather to charge the rapid discharge capacitors represented by C_2 which are the EMP source. The multi stage impulse generator is henceforth denoted as the primary generator circuit and the rapid discharge capacitor C_2 and external spark gap G_2 denoted as the secondary generator circuit.

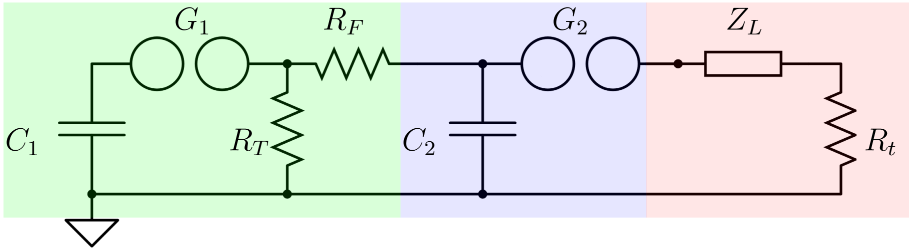

Figure 2.2: Simplified electric circuit model of an impulse generator with a rapid discharge circuit and a TL with a termination resistor

Notice the absence of front and tail shaping resistors in the rapid discharge circuit in Figure 2.2, the reason for this is to not introduce any additional component slowing down the front time. There will naturally be a finite resistance occasioned by resistivity in the conductors and parasitic resistance at contact points. Even though design efforts to reduce stray inductance, a finite stray inductance that also slows down the pulse naturally is inevitable.

One key factor that enables a more compact design of the rapid discharge circuit is the influence of the steepness of the voltage front, or in other words the electric field derivative, on the breakdown voltage. For steeper fronts, higher voltage stress can be applied to an air gap before it breaks down. The explanation of this phenomena is that a conducting channel causing a breakdown in an previously insulating air gap can not develop instantaneously. It takes some time, commonly referred to a as statistical and formative time-lag, for a streamer discharge to expand such that it stretches the complete air gap and eventually causes a breakdown. This means clearances can be reduced in the secondary circuit compared to primary circuit as the secondary circuit will have shorter rise time and FWHM.

2.1.2 Spark gap trigger mechanism for impulse charging

With the generator setup presented in Figure 2.2 there is no need for a dedicated pulse trigger system in G_2. Assuming G_1 has a functional pulse trigger system, for example a spark plug, the spark gap G_2 can be triggered automatically once G_1 have been triggered causing an increased voltage stress over G_2 spark gap. The voltage impulse amplitude generated by primary generator circuit in combination with the breakdown voltage of spark gap G_2, can be set such that G_2 triggers automatically. This means the voltage impulse generated from the primary generator circuit is chopped. As the fundamental physics of electric discharges include statistically dependent events, the breakdown voltage has a certain statistical variation.

Adjusting the generated pulse voltage amplitude in the primary generator circuit or the breakdown value of G_2 such that the pulse is front-chopped gives less variations in breakdown voltage compared to peak-chopping och tail-chopping. The reason for this behaviour is that for front-chopping the voltage stress will certainly exceed the dielectric strength of the gap by large margins, shortening the time duration where voltage stress is close to V_{bd}, which makes the impact of statistical variations less prominent. Another factor that reduces the spread of the breakdown voltage is a homogeneous electric field in the spark gap.

A conducting spark gap is not an ideal conducting channel as it has a nonzero series resistance. The results presented in [10] indicates that the spark gap length is a determining factor for the resulting spark gap resistance. To keep the spark gap resistance low, the spark gap distance should be minimised.

The disposable variables affecting spark gap breakdown voltage are gas type, gas pressure and gap distance. Two commonly used insulation gases are air and sulphur hexafluoride (SF6). Advantages of air are easy accessibility and gratuitous to use. SF6 is a gas of great electrical properties such as high electron attachment coefficient giving high dielectric strength but having a global warming potential 23,900 higher than carbon dioxide the environmental impact is severe if emitted into the atmosphere. Therefore, one should strive for using alternative gases when possible. If SF6 is to be used the leakage should be minimised and the gas recycled. An approximate model for determining the ignition voltage leading to breakdown in a spark gap is

$$V_{bd} = k_1 pd + k_2\sqrt{pd} \tag{2.7}$$

where k_1 and k_2 are gas specific constants [7]. Numerical values of these constants are presented in Table 2.1 and used to plot (2.7) in Figure 2.3.

gas	k_1 [kV/(mm bar)]	k_2 [kV/($\sqrt{\text{mm bar}}$)]
Air	2.43	2.01
SF6	8.8	0.27

Table 2.1: Numerical values of gas specific constants to be used in (2.7) for calculating spark gap ignition voltage [7].

As observed in Figure 2.3, the product of pressure and distance needs to be much higher in air compared to SF6 for obtaining the same breakdown voltage. The physical explanation is different electrical properties of the gases.

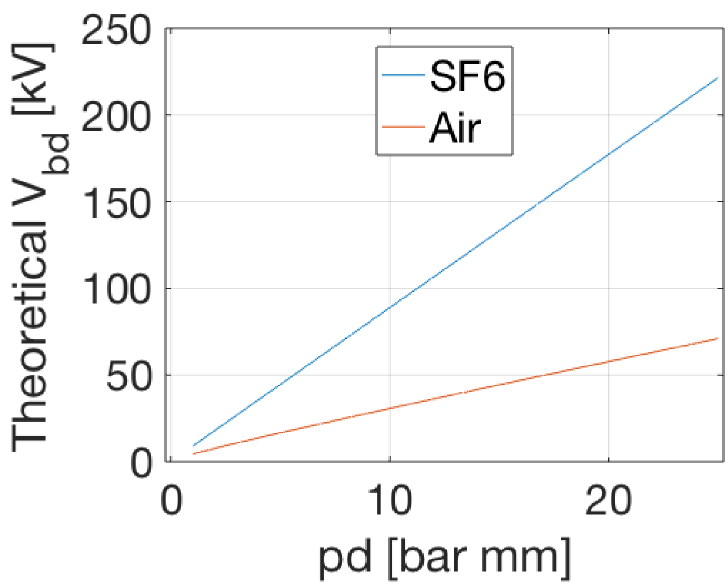

Figure 2.3: Theoretical breakdown voltages for spark gap in air and SF6 gas as function of the product of gas pressure and spark gap distance.

To use other conditions than ambient air, a vessel enclosing the spark gap and the gas at desired pressure level is needed. The higher pressure, the higher mechanical strength of the vessel is required. Further demands on the vessel is that it needs to be manufactured from electrically insulating materials to make the spark gap electrodes electrically insulated from each other when the spark gap is not ignited.

2.1.3 Spark gap trigger system for DC charging

Instead of using impulse charging with automatic triggering mechanism for the spark gap in the secondary generator circuit, DC charging and a dedicated pulse trigger system could be used. A simplified electric circuit diagram for an EMP generator with DC charging of the generator capacitors is shown in Figure 4.21. Three alternatives for spark gap trigger system are presented in the following paragraphs.

The first option is to install a spark plug at the tip of the spark gap electrode to generate an igniting spark. This requires an electric control circuit, an amplifier to amplify signal from control circuit to a spark plug, to practically fit and install a spark plug and a pressure proof cable lead-through into the vessel. Hence, this option have several advanced practical challenges that need to be addressed.

The second option is to use high pressurised air instead of SF6. If using air, it would be possible to dump the gas into surrounding environment. In case of SF6 a compressor and recycling unit is needed to empty the vessel from SF6. Filling and refilling require moving connection of gas hoses between every EMP which is impractical and time consuming.

The third possible alternative for trigger system is without a need for a pressurised vessel and instead using three metal sphere electrodes. Two of them are fixed in position, one connected to the rapid discharge capacitors and the other connected to the transmission line. The air gap between these two spheres should sufficiently long to not break down. A third sphere is placed on a runner and slided into position between the two other by either a mechanical spring or a pneumatic system resulting in two succeeding air gap breakdowns. Possible drawbacks of this option is that multiple spark gap most could increase the total series resistance of the trigger system.

2.2 Electromagnetic waves

For high frequency (HF) signals the electric and magnetic fields are changing rapidly and could be described using theory of travelling waves. Maxwell's equations are central in describing the fundamental physics. Presented in their integral form, the Maxwell's equations are given as

$$\oint_C \vec{E} \cdot d\vec{l} = -\frac{\delta}{\delta t} \iint_A \vec{B} \cdot d\vec{A} \tag{2.8a}$$

$$\oint_C \vec{H} \cdot d\vec{l} = \iint_A (\vec{J} + \frac{\delta}{\delta t}\vec{D}) \cdot d\vec{A} \tag{2.8b}$$

$$\oiint_A \vec{B} \cdot d\vec{A} = 0 \tag{2.8c}$$

$$\oiint_A \vec{D} \cdot d\vec{A} = Q \tag{2.8d}$$

where (2.8a) is Faraday's law, (2.8b) is Ampère's law, (2.8c) is the law of no magnetic monopoles and (2.8d) is Gauss's law. The used notations in (2.8) are; $\vec{E}$ is electric field vector, t is time, $\vec{B}$ is magnetic flux density vector, C is the closed path along $d\vec{l}$ for which the line integral is evaluated and the curve C is also enclosing surface A, $\vec{H}$ is magnetic field intensity vector, $\vec{J}$ is current density vector, $\vec{D}$ is electric displacement field vector and Q is electric charge. The relation between some of these presented quantities are gives by the constitutive relationships stating that

$$\vec{D} = \epsilon \vec{E} = \epsilon_r \epsilon_0 \vec{E} \tag{2.9}$$

where ϵ is the permittivity, $\epsilon_0 = 8.85 \times 10^{12}$ [F/m] is the permittivity of vacuum, ϵ_r is the unitless relative permittivity of a material or medium and

$$\vec{B} = \mu \vec{H} = \mu_r \mu_0 \vec{H} \tag{2.10}$$

where μ the permeability, $\mu_0 = 4\pi \times 10^{-7}$ [H/m] is the permeability of vacuum, μ_r the unitless relative permeability of a material or medium. The way EM waves travel in time and space are described by (2.8a) and (2.8b) . Combining the differential form of these equations and using vector algebra, one can derive Helmholtz wave equation in source free medium as

$$\nabla^2 \vec{E} - \frac{1}{c} \frac{\delta^2 \vec{E}}{\delta t^2} = 0 \tag{2.11}$$

where c is the speed of light defined as

$$c = \frac{1}{\sqrt{\epsilon \mu}} \tag{2.12}$$

giving an approximate speed in air as $c_0 \approx 3 \times 10^8$ m/s $= 0.3$ m/ns [11]. Information quantifying the properties of such travelling waves are direction of propagation, eventual superposition, polarisation and medium in which the wave propagates. Ather solving (2.11) one can use differential form of (2.8a) to find a simple relationship between electric and magnetic field. The fields $\vec{E}$ and $\vec{B}$ will be perpendicular to each other and the ratio for waves propagating in air domain is

$$Z_{wave} = \frac{E}{H} = \sqrt{\frac{\mu_0}{\epsilon_0}} = 377\ \Omega \tag{2.13}$$

where Z_{wave} is denoted as the characteristic impedance of free space.

2.2.1 Transmission lines characteristics

In previous section, wave propagation for any arbitrary direction was described. To control the direction of propagation and to make an efficient point-to-point interconnection TLs can be used. Properties affecting TL characteristics are wave frequency, size and geometry of TL and dielectric substrate . Examples of arrangement of TLs are coaxial, microstrip, parallel plate and stripline. The characteristic impedance of a TL is denoted Z_L and is not to be confused with wave impedance in (2.13). TLs can be modelled with per length value of resistance R', inductance L', capacitance C' and conductance G'. An equivalent electric circuit for a TL with two conductors, one energised and one grounded, is shown in Figure 2.4 where $\hat{z}$ is a unit vector in the cartesian coordinate system.

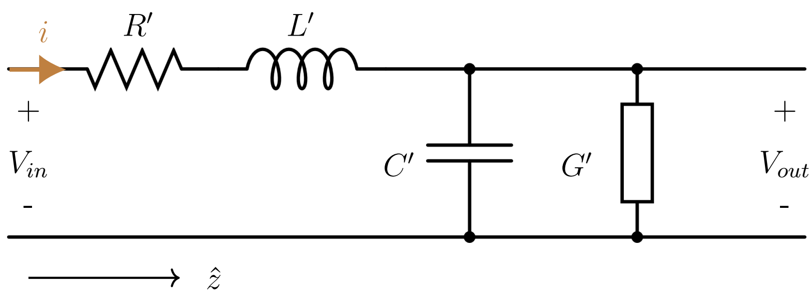

Figure 2.4: Two port electric circuit model of a TL.

Applying Kirchhoff's current and voltage law on the equivalent circuit in Figure 2.4 give the differential equations known as "the general transmission line equations" or alternatively, "the telegrapher's equations". When describing voltage and current using phasor notation for $V(z)$ and $I(z)$, these equations can be written as

$$-\frac{dV(z)}{dz} = (R + j\omega L)I(Z) \tag{2.14a}$$

$$-\frac{dI(z)}{dz} = (G + j\omega C)V(Z) \tag{2.14b}$$

which are known as the time-harmonic transmission line equations where $\omega = 2\pi f$ [rad/s] represent the signal frequency. The approach for obtaining a general solution to these equations is to consider the resulting wave as a superposition of one forward and one backward travelling wave as

$$V(z) = V^{+}(z) + V^{-}(z) \tag{2.15}$$

where V^{+} is the incident/forward travelling wave, V^{-} is the reflected/backward travelling wave.

The characteristic impedance, defined in standard manner as the ratio of voltage and current, of a TL con be derived from (2.14) as

$$Z_L = \sqrt{\frac{R' + j\omega L'}{G' + j\omega C'}} \tag{2.16}$$

where j is the imaginary unit of a complex number. When a TL is approximated as being lossless, (2.16) is simplified to

$$Z_L = \sqrt{\frac{L'}{C'}} \tag{2.17}$$

which means the characteristic impedance of a lossless TL can be found from its inductance and capacitance value only.

One category of TLs is the *microstrip* which consist of two parallel plates with arbitrary width. Analytic expressions for characteristic impedance of microstrip with ϵ_r=1 have been suggested in literature as

$$Z_L = 60\ln(\frac{8h}{W} + \frac{W}{4h}) \quad \text{if } \frac{W}{h} \leq 1 \tag{2.18a}$$

$$Z_L = \frac{120\pi}{\frac{W}{h} + 1.393 + 0.667\ln(\frac{W}{h} + 1.444)} \quad \text{if } \frac{W}{h} > 1 \tag{2.18b}$$

where ln is the natural logarithm, W is width of energised conductor and h is separation between strip conductor and ground plate [12]. Equation (2.18) does not specify the width of the grounded plate. The inflence on the characteristic impedance from the ground plane width have been investigated by [13]. It was concluded that $\frac{W_g}{W} \geq 3$, where W_g is ground plane width, is required for microstrip equations to be valid. For heavier truncated ground plane width, i.e. for $\frac{W_g}{W} < 3$, the characteristic impedance of the TL increases.

A so-called *Parallel plate* structure could be considered a special case of microstrip where the conductor and the ground plane are of same width. Analytic expressions of inductance and capacitance of a parallel plate TL that assumes infinite width of plates, i.e. no fringe effects are considered, can be derived from (2.8a) and (2.8d) respectively are given as

$$L' = \mu \frac{h}{W} \tag{2.19a}$$

$$C' = \epsilon \frac{W}{h} \tag{2.19b}$$

where L' [H/m] and C' [F/m] is the per length unit inductance and capacitance respectively. Inserting (2.19) into (2.17) yields

$$Z_L = \frac{h}{W}\sqrt{\frac{\mu}{\epsilon}} \tag{2.20}$$

which means the characteristic impedance of a TL can easily be manipulated by adjusting its geometry.

2.2.2 Impedance matching and reflecting waves

When analysing EM wave propagation, the characteristic impedance of the TL and the dielectric medium in which the wave propagate are important parameters. If the medium is air everywhere, the impedance of free space applies which has been given in (2.13). Fundamental wave theory tells that any discontinuity in characteristic impedance of TL results in reflection of a part of the incident wave. For a wave that is conducted by a TL with impedance Z_{L1} that hits a point where impedance changes to Z_{L2} the reflection coefficient is given as

$$\Gamma = \frac{Z_{L2} - Z_{L1}}{Z_{L2} + Z_{L1}} \tag{2.21}$$

and the transmission coefficient at the same point is given as

$$T = 1 + \Gamma \tag{2.22}$$

where both Γ and T are unitless. As a fraction of the wave is reflected back, the general solution is consider a travelling wave as a superposition of several waves, see (2.15), in order to obtain a model that fulfils all present boundary conditions.

A common way of describing HF voltage waves is by using scattering parameters (S-parameters) applied on an electric circuit of several ports. For a two-port circuit, one input/excitation port and one output/termination port, two of the S-parameters can be linked to voltage and impedance expressions in (2.15) and (2.21) respectively. If the input port is denoted with subscript one and output port denoted with subscript two the S-parameters are calculated by

$$S_{11} = \frac{V_1^-}{V_1^+} = \Gamma \tag{2.23a}$$

$$S_{21} = \frac{V_2^-}{V_1^+} = T \tag{2.23b}$$

and are linked to the reflection and transmission coefficient as indicated [14].

Having matched TL terminations, meaning $\Gamma = 0$, is desired in many applications. In an EMP simulator, a TL termination needs to withstand the voltage stress level of the EMP and also be able to dissipate the pulse energy. Designed with proper dimensions, a water resistor could be capable of meeting these demands. An advantageous feature of a water resistor is that its resistance value easily can be changed by using a solution of water and salt and varying the salt concentration, meaning the a water resistor can be adopted to TLs of different characteristic impedance. Using a water solution with sodium carbonate a conductivity, σ, up to 103,000 μS/cm can be obtained [15]. The resistance, R, of a water resistor is calculated using the general equation

$$R = \frac{l_R}{A_R \sigma} \tag{2.24}$$

where l_R is the through water length of the resistor and A_R is the cross section of the water resistor.

2.2.3 Properties of field derivative sensors

To measure electric field either a D-dot sensor or a B-dot sensor can be used. The signal from a D-dot sensor should give the derivative of the electric displacement field while the signal from a B-dot sensor should give the derivative of the magnetic flux density. The electric field is obtained by integrating the signal from the D-dot sensor and applying (2.9). To obtain the electric field from a B-dot, the sensor signal should first be integrated and then (2.10) and (2.13) used. A D-dot sensor can have the structural characteristic of either monopole or dipole antenna. The geometry of a D-dot sensor have decisive impact on its performance in terms of bandwidth and linearity. The results from [16] indicate that for monopole D-dot sensors, the length and thickness of the monopole antenna affect the sensitivity of the sensor. The thicker and longer extrusion of the monopole antenna from the ground plane it is mounted to, the higher amplitude in the measured signal was observed. A B-dot sensor is basically a loop antenna where the loop size influences sensor performance.

The authors of [17] have developed an equivalent electric model for a D-dot sensor with a transfer function from electric field to sensor voltage output described as a high pass filter. For Em fields of frequencies below the cutoff frequency of the sensor its output voltage, V_s is proportional to the derivative of the electric field

$$V_s \propto \frac{dE}{dt} \tag{2.25}$$

given that $\epsilon_r = 1$ of the surrounding medium.

2.3 Properties of radiation system geometries

There are several types of radiation systems geometries that could fulfil the requirements of test standard *MIL-STD-461G RS105* which calls for either a TEM cell, parallel plate transmission line or any other equivalent radiation system. An overview of the possible radiation system geometries is shown in Figure 2.5 where grounded parts are displayed in black, parts of high potential are displayed in grey and EUT is displayed in brown.

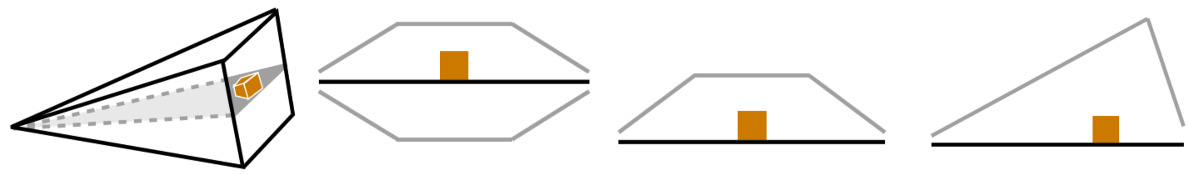

(a) GTEM cell. (b) Open TEM cell. (c) Parallel plate. (d) Triangular shape.

Figure 2.5: Sketches of different types of radiation system geometries for RS testing.

Figure 2.5b displays the geometry of an open TEM cell, also called TEM cell, triplate or symmetric stripline. An open TEM cell have a structure of three conducting plates, the middle one (septum plate) is energised and the top and bottom plates are grounded. A drawback is that the septum plate need to be elevated and have the mechanical stability to hold the EUT. Close to the signal input and termination ends, the top and bottom plates are inclined symmetrically around the septum plate in the middle. There is a part where all three plates are horizontal and parallel where the EUT is intended to be placed. One manufacturer of TEM cells states that operational frequency range is up to 3 GHz but having optimal performance up to 1 GHz only[18]. The characteristic impedance of an open TEM cell is half of the characteristic impedance of a parallel plate of corresponding size [19]. Several design aspects for TEM cells are mentioned in [20]. One notable thing is that the inclined part of top plate could cause distortions, the steeper inclination the more undesired distortions. The separation distance between plates is a key design factor as the cut-off frequency seems to be inverse proportional of the separation distance [20].

A suggested alternative to the open TEM structure is a so-called Gigahertz transverse electromagnetic cell (GTEM cell) shown in Figure 2.5a. A GTEM cell features an enclosed test environment as it is enclosed by electrically conducting grounded walls shaped like an pyramidally expanding coaxial line with an inner energised septum plate. The enclosed environment ensures that no interfering signals can be injected into the test environment and also that no signals leak out to the surroundings decreasing the needed safety distance. The input is located at the pointy end and there are RF absorbers in the opposite end to mitigate reflections. One manufacturer of GTEM cells promises an operational range up to 20 GHz but only optimal performance up to 1 GHz [21]. One significant difference to an open TEM cell is the resulting electric field distribution as a GTEM cell also features grounded vertical walls.

Another radiation system design is a simple parallel plate structure with two horizontal plates, the upper one energised and the lower one grounded. To enable practical input and output TL terminals, the top plate is inclined in the end regions such that the plates are brought closer to each other at the terminals. The impact on the electrical performance from the steepness of the inclined sections has been analysed by [22]. The author suggest that the steepness (referred to angle α in Figure 1.1) should not exceed 30 ° to not introduce additional reflections at this point. A benefit compared to both an open TEM cell and a triangular shaped is that it occupies less space in vertical direction and less material is required making the parallel plate geometry more cost-effective.

A design that could be regarded as an equivalent radiation system design in *MIL-STD-461G RS105* is a triangular structure suggested by [23]. It features one ground plane and a top plate of two inclined sections. The authors claim that this design is preferable to the parallel plate structure as this distorts the pulse shape. One drawback though is that the top point of the radiation line is more elevated compared to the parallel plate geometry for the same usable test area. Consequently a triangular TL geometry requires increased clearance as mentioned in Section 1.1.1.

2.3.1 Conductor types for radiation system

Possible alternatives for conductors in the radiation system are conducting wires, tubes, sheets of nets. Of the different geometries presented in Figure 2.5, only the GTEM cell technically needs fully covering sheets to be used as walls. For other geometries in Figure 2.5b-2.5d a meshed net or wires can be used instead of sheets covering the complete surface. If the used net have sufficiently fine mesh or the wires are placed close enough to each other this could be equivalent to use solid sheets in electrical terms. Radiation system designs using wires and sheets as conductors respectively, for a parallel plate geometry TL, are visualised in Figure 2.6.

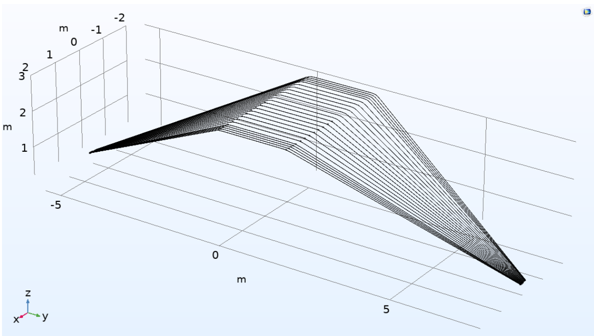

(a) Transmission line with conducting wires.

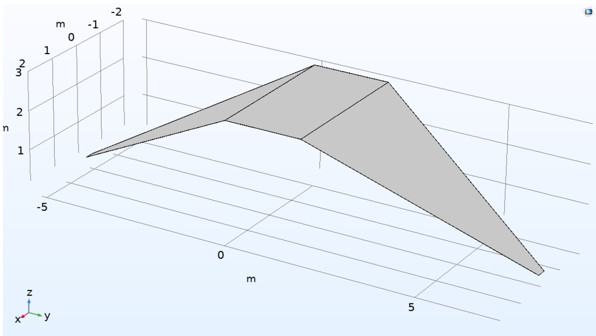

(b) Transmission line with conducting sheets.

Figure 2.6: 3D model visualisation of parallel plate transmission lines.

3 Method

This chapter presents the procedures carried out to achieve the goals in this project. A thorough perusal of *MIL-STD-461G*, with emphasis on chapter ”RS105”, was initially done to obtain knowledge of technical requirements of the test standard. Comsol multi-physics, mainly electrostatic interface in AC/DC module but also RF interface, was used for FEM simulations in the design process. Construction work was done with support from RISE metal workshop and the complete testbed was installed in RISE HV laboratory. The performance of the testbed was evaluated with respect to given specifications in *MIL-STD-461G RS105*.

3.1 Design choice of radiation system geometry

Based on the review of radiation system geometries presented in Section 2.3 a parallel plate TL structure was chosen. It was believed that cell type geometries would be preferred for smaller TLs where high bandwidth is required. However, as TL size required to perform ”RS105” tests with a EUT size 1x1x1 m^3 is large this design was considered impractical mainly because of the numerous large metal sheets that would be needed. The total TL length in y-direction (see Figure 1.2) was set sufficiently long to delay eventual reflections from TL termination to prevent pulses from superimposing and thus prolonging FWHM time. The length of the inclined part of TL, see l_2 in Figure 1.1b, was maximised to make the angle α, see Figure 1.1a, as small as possible. A positive aspect of this design choice is that the horizontal components of the electric field radiated from the TL are kept as low as possible which is preferred as the goal is to have a purely vertical electric field in the test volume. The length of the top, flat horizontal, part of TL was set to the minimum value demanded by the test standard as simulations showed no advantages in terms of increasing this distance.

At an early stage of this project, different radiation system geometries shown in Figure 2.5 were compared. Even though electrical performance was prioritised, the radiation system also needed to be practical to install and operate. The GTEM cell was undesired due to its more complex design with RF absorbers and more inconvenient usability in a enclosed testbed environment. The open TEM cell would occupy a lot of space in vertical direction due to the use of two planes at high potential. The elevated input port would also need an elevated position of the EMP generator and and an extra (elevated) ground plane would have to be introduced. The parallel plate and ”triangular” shaped radiation systems were considered having simpler designs in comparison to GTEM cell and TEM cell. As the parallel plate geometry theoretically should provide constant electric field intensity in the usable test volume and require smaller total height and clearance for TL, this design is preferred instead of the triangular geometry. Thus, the firsthand choice was the parallel plate structure and simulations were performed to verify that this design could fulfil the test standard requirements.

The design choice of having wires as conductors was favoured rather than sheets as the design with wires was believed to be more flexible for adjusting transmission line dimensions. Furthermore, it was suspected that sheets of sufficient thickness to not be brittle would be too heavy to be easily handled. The chosen TL conductor wire type was a braided tin plated copper sleeve with a diameter of 4 mm. It had a plastic former inside helping to maintaining its round shape.

3.2 Parameters of EMP generator circuit

In this project, impulse charging of EMP generator capacitors was applied. An ASEA marx generator was the only suitable HV generator to charge the GA capacitors available at RISE HV laboratory. In the absence of a suitable DC charging source at the moment of this project, DC charging was unfortunately not an option. To construct or purchase a DC source were out of the thesis scope and budget.

An electric circuit model of the EMP generator is presented in Figure 2.2. The values of the circuit components in the EMP generator, unless nothing else stated in conjunction with presented result, were; C_1=110 nF, R_1 = 75 Ω, R_2 = 250 Ω, C_2=4 nF. The front and tail resistor values (R_1 and R_2) was chosen too give as fast impulse as possible while at the same time not stressing the ASEA generator too much. Here C_1 represent the equivalent capacitance of the ASEA marx generator when two stages of 220 nF each were used and C_2 represent the equivalent capacitance of two series connected General Atomics (GA) capacitors of 8 nF ± 10 % each. The GA capacitors are rated 100 kV and have an equivalent series resistance of 6 nH each. The GA capacitors were connected in series throughout all experimental tests giving a total voltage rating of 200 kV and an equivalent series inductance of 12 nH.

3.3 Execution of COMSOL Multiphysics simulations

Various different softwares for performing numerical solutions to physics related field problems are available. COMSOL Multiphysics is a finite element method (FEM) based software for modelling and solving electromagnetic problems among other applications. The principle is that, by using FEM the model is discretized and the governing differential equations are solved. In the modelling process, the problem was described as a boundary value problem using boundary conditions.

Several different simulations were performed. The electrostatics interface was used to evaluate the dimensions of the TL in terms of produced electric field. To fully resemble the field distribution for an emitted EMP, simulations in time domain would be needed. Modelling in time domain would have required analysing result of multiple time-points and more computational power to perform simulation slowing down the design process. Instead, electrostatic interface was chosen as these simulations could easily provide an approximate overview of the field distribution in space and still give an adequately representative way of comparing TL design and dimension. The TL and the HV laboratory environment was modelled in these simulations. An outline of the parallel plate TL is shown in Figure 1.1 including denoted length parameters. Simulation results were used to determine the values of these parameters. Moreover, the impact of having either wires or sheets as TL conductors, as displayed in Figure 2.6, was simulated and evaluated.

The RF interface in Comsol was also used to analyse the wave propagation and the characteristic impedance of the TL. This was done for the same TL geometry that was used in electrostatic simulations. In frequency domain, two "lumped ports" were used to excite a voltage and to terminate the TL respectively. Furthermore, the impact of the value of the angle α (from Figure 1.1) was simulated in Comsol RF interface. Using Comsol RF module, the S-parameters defined in (2.23) were computed and used as comparative value in the analyse of the simulation results .

3.4 Practical preparations in HV laboratory

The intended premises for the EMP testbed was RISE HV laboratory in Borås. The laboratory had grounded floor, walls and ceiling which had to be taken into account for the resulting field distribution. A way to elude these concerns would to simply perform the EMP tests outdoors. However, with no mobile HV source at hand the testbed had to be set up indoors. The size of HV laboratory was almost large enough to fulfil the recommended safety clearance to surrounding walls and ceiling stated in "RS105". Recommended clearances could not be maintained to some voltage dividers and capacitors present in the laboratory but not being used in the testbed. The recommended clearances was believed to rather target the impact on field distribution than a safety issue. It was ensured that these passive devices were grounded and shortened in order to avoid residual voltages and that clearances were sufficient from a safety perspective. However, the presence of these devices at ground potential relatively close the TL might have caused undesired field distortions. Additionally, there were control units containing active electronic components present in the lab. The risk of causing damage to these active components were minimised by placing them at recommended safety distance inside shielding metal boxes.

3.4.1 Construction work and assembly

The HV laboratory floor was made of concrete and with ground potential accessible via copper connection plates with a radius of 3 cm placed in a quadratic mesh with the nodes distanced two meter 2 m from neighbouring nodes. These connection plates also had internal M10 threads enabling mechanical fixture of objects using bults. Even though the HV laboratory floor was already grounded, an additional grounded plane was introduced. This was done because the original laboratory floor ground was done with a copper net buried approximately 10 cm deep into the concrete floor. This was done to ensure the EM wave travel in air only and not in any other material, i.e. concrete, with another value of relative permittivity. An electrically conducting steel net of size 4.6 x 20 m was placed on the concrete floor and attached mechanically and with a firm electric contact to the grounding nodes.

A mechanically supporting wooden frame was built to keep the TL wires steadily fixed in a parallel plate structure and, at the same time, tensioning the wires to avoid sag. Wood was considered the most practical material choice as it is easy to handle, provides electrical insulation and is inexpensive. As the wooden frame was placed in the volume of EM wave propagation it might have some influence on the TL performance. To get a controlled and repetitive field distribution in the TL it was assured that all conducting objects in the testbed was either at high potential or grounded, i.e. no objects were left at floating potential. Consequently, metal screws that would have been a robust and simple solution for the fixture of the wooden frame could not be used. Instead of metal screws, nylon threaded bars, washers and nuts was used at intersection points between studs in the wooden frame.

3.4.2 Managing of the EMP testbed

After finalising the assembly of the testbed, the spark gap vessel was pressurised. First a vacuum compressor was used to evacuate the air from the vessel. SF6 gas was then filled into the vessel up to desired pressure level. A SF6 tube and the spark gap vessel was connected to a dedicated SF6 pump system via hoses. The SF6 system had to be disconnected from the vessel when operating the testbed. Thus fine tuning the vessel pressure to obtain the desired flashover voltage in the spark gap was very time consuming as hoses had to be reconnected every time pressure should be increased or decreased. The SF6 system included a vacuum compressor and a recycling and gas cleaning unit so that the SF6 gas could be filled back into the tube again. Even though being very caution when handling the SF6 some leakage occurred when disconnecting hoses and during long time storage of pressurised gas inside the vessel.

The ASEA marx generator was set up and connected to the rapid discharge circuit. For details of the Marx generator circuit parameters, see Section 3.2. Initially the generated voltage impulses had an amplitude less than half of the target amplitude of 180 kV and the charging voltage was increased in steps. This was done as a safety precaution and as an attempt to avoid external flashovers and overcharging of capacitors in case of unsuccessful pulse triggering in the rapid discharge circuit or voltage reflections.

3.5 Setup of measurement system

The measurement system was set up mainly by existing calibrated measurement equipment at RISE including high voltage dividers and an oscilloscope. All measurement data was saved onto computers via fibre optic communication links and post-processed in Excel and Matlab. The data acquisition process included multiple manual actions of exporting/importing data and calculation of rise times etc making it time consuming. Additionally, simple self-made field derivative sensors were used. The acquired field derivative sensor data was integrated digitally in the post-processing work and amplitude normalised.

3.5.1 Measurement equipment used in the EMP testbed

The main measurement data acquired in the EMP testbed were

- Output voltage from primary generator circuit which is applied to the GA capacitors. This voltage was measured using a Passoni Villa HV divider.
- Output voltage from secondary generator circuit. This voltage was measured to verify ignition of spark gap and that voltage impulse was properly passed on to the TL. This voltage was measured using a PIKA VFT600 HV divider.
- Electric field derivative and magnetic field derivative in the intended test volume.

It was preferred to have these three measurements sampled synchronously to get the time order of observed events. This was simply accomplished by connecting all measurement devices to the same oscilloscope. A Tektronix DPO7254 oscilloscope was used. In the results presented in Section 4.3, compensation have been made for the time delays for signal propagation in measurement cables. A sample rate of 10 GS/s was used as this should give enough resolution on the front of EMP. External signal attenuators were connected in between measurement cables and oscilloscope input to ensure voltage level would not exceed the rated level of oscilloscope's input channels. The scale factors presented in Table 3.1 are the total scale factors for the HV divider together with the used external attenuators.The custom made fields sensors used are displayed in Figure 3.1 were not calibrated. Consequently the sensor scale factor k_s, see (2.25), was unknown and the sensor is unable to provide information about absolute value of electric field. However relative amplitude differences in field sensors signal measured from different EMPs can be analysed. To avoid confusions about the scale factor k_s, the field sensor signals presented in Section 4.3 are amplitude normalised.

Measurement device	Field sensor	PIKA VFT600 HV divider	Passoni Villa HV divider
Scale factor	k_s	95,525	101,652
Oscilloscope channel input impedance [Ω]	50	50	10^6
Oscilloscope channel BW [GHz]	2.5	2.5	0.5
Measurement cable type	Megaphase Warrior cable	Ecoflex 10 plus	Bellden 7801A
Measurement cable length [m]	10	17.8	5
Propagation speed factor (ratio to speed of light)	0.61	0.85	0.81

Table 3.1: Technical data for measurement cables and oscilloscope data acquisition settings.

All the used field sensors were mounted onto a 3x70x70 mm aluminium plate and are presented in Figure 3.1.

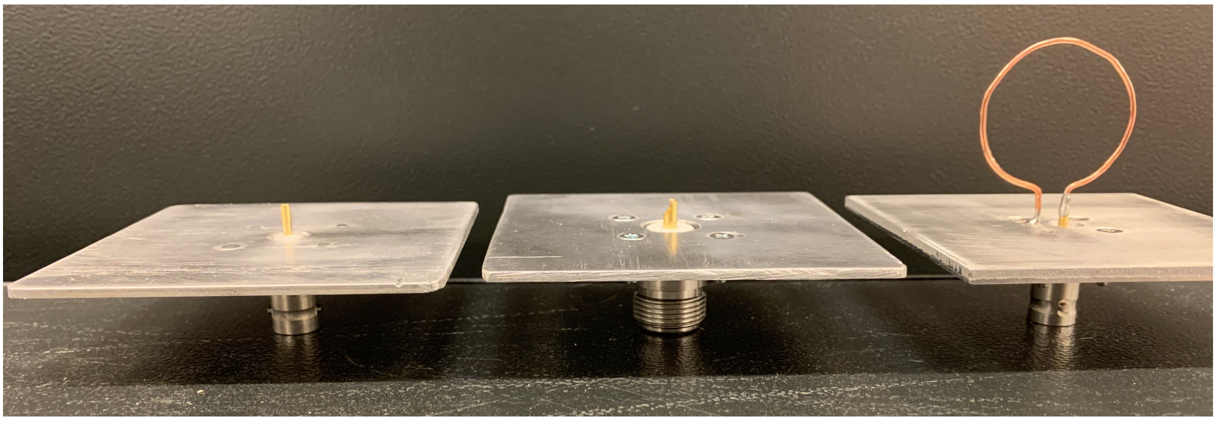

Figure 3.1: Field sensors used in the EMP testbed. From left: D-dot sensor with BNC contact, D-dot sensor with N-type contact, B-dot sensor with copper circular loop of 3 cm diameter.

4

Results and discussion

In this chapter, results from performed Comsol simulations are presented and the design choices these simulations lead to. Further, an overview of the constructed testbed and detailed views of some of its parts are displayed. Furthermore, the measurements and results from experimentally tests are presented and discussed. Finally recommendations of future work and suggested improvements of the EMP tested are presented.

4.1 Comsol simulation results

This section presents results from simulations in Comsol multiphysics, mainly from electrostatic interface and but also from RF interface.

4.1.1 Simulation of electric field distribution in radiation system

In Figure 4.1, the simulated electric field norm is shown in the coloured surface plot with associated colour range. The magenta line emphasises the border line where electric field is 50 kV/m which is the minimum level required by the test standard. As seen in the figure, the region where $|E| > 50$ kV/m stretches from x-coordinate -1.3 m to +1.3 m enabling a theoretical test object width of 2.6 m giving good margin to desired one metre width. The arrows show normalised electric field. The black lines represent the TL part being at high potential. The grey lines show the contour of the maximum size of an intended EUT, for details see Section 1.1.1.

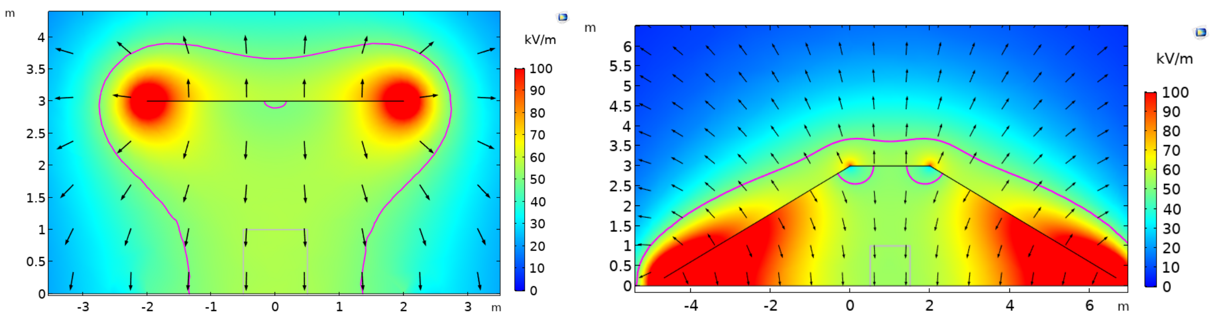

(a) View of a cut xz-plane (b) View of a cut yz-plane

Figure 4.1: Simulated electric field distribution from parallel plate TL with conducting sheets at 165 kV.

A model the TL in 2D xz-plane was used to analyse impact of having individual wires as conductors instead of sheets. A 2D simulation setup requires, even though having finer mesh resolution, less computational power compared to 3D even though having finer mesh giving a better accuracy. One obvious disadvantage of using a 2D model is lost information of how object in the third dimension affects. Note that no geometric symmetry was utilised in this transition of 3D modelling to 2D modelling, hence information was lost. However, as the EMP would travel along the TL in time domain, this 2D simulation could resemble the time-point when the pulse peak passes the centre point of the TL. Thus, this 2D model was believed to provide good comparison between wires or sheets as conductors as a very fine mesh could be applied in the FEM discretization. A 2D electrostatic simulation of electric field distribution for a TL with conducting wires, with an otherwise same geometry as in Figure 4.1a, is presented in Figure 4.2. The simulation showed that a voltage of 180 kV was needed, compared to 165 kV for simulation with sheet conductors, to obtain electric field intensity above the threshold value of 50 kV/m in a sufficiently large volume.

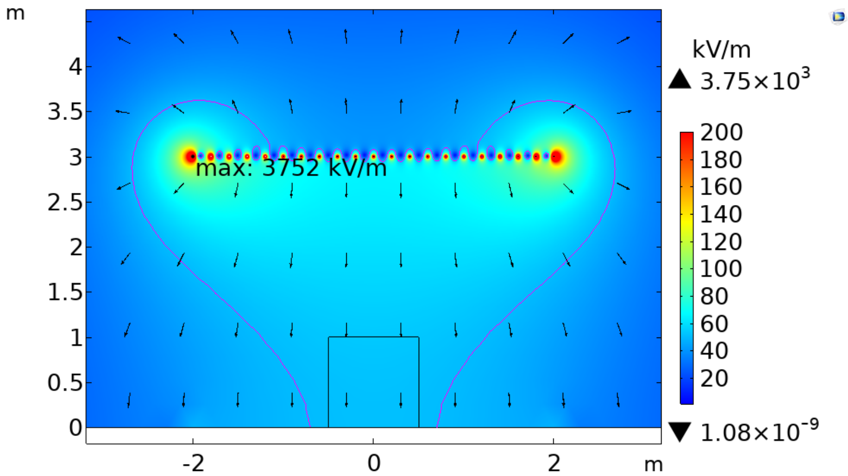

Figure 4.2: Simulated electric field distribution in TL for 21 geometrical evenly distributed conducting wires at a voltage of 180 kV, view in xz-plane.

4.1.2 Simulations of TL bandwidth and characteristic impedance

In Comsol Radio Frequency (RF) interface, frequency domain simulations were performed. Figure 4.3 presents simulation results of the influence of the TL angle α, see Figure 1.1a, on its performance. The result indicate a larger attenuation for larger α in line with the findings of [22] presented in Section 2.3. From simulation result, the indicated TL bandwidth range from 120 MHz to 180 MHz for $\alpha = 60°$ and $\alpha = 30°$ respectively.

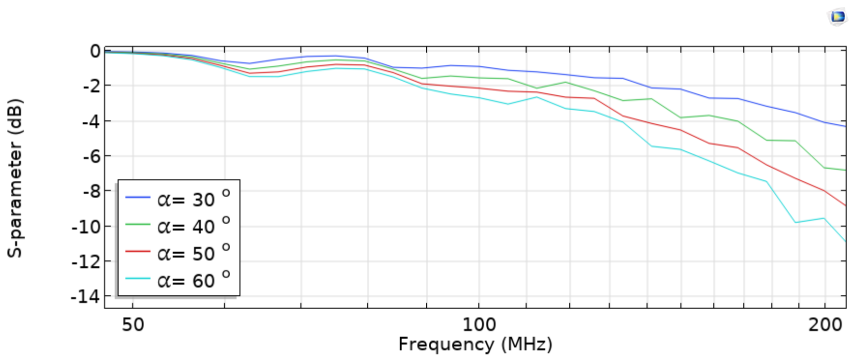

Figure 4.3: Simulated frequency sweep of S21 parameter for different steepness of inclination (angle α) of inclined sections in the TL.

In Figure 4.4 simulations of TL S-parameters are shown. Two different boundary conditions; Perfect magnetic conductors (PMC) and perfect electric conductors (PEC) were used to model laboratory walls and ceilings. The PEC condition was believed the most accurate to model the conditions present in the lab while PMC might be more representative for an open area test site. A sweep of the input and output impedance was done to find how this affected the S-parameters and thereby find the value providing best impedance matching. The part of interest is where S11 has the highest negative peak and where S21 is closest to the zero level. Looking at Figure 4.4a the best value for impedance matching seems to be 105 Ω and from Figure 4.4b 135 Ω respectively.

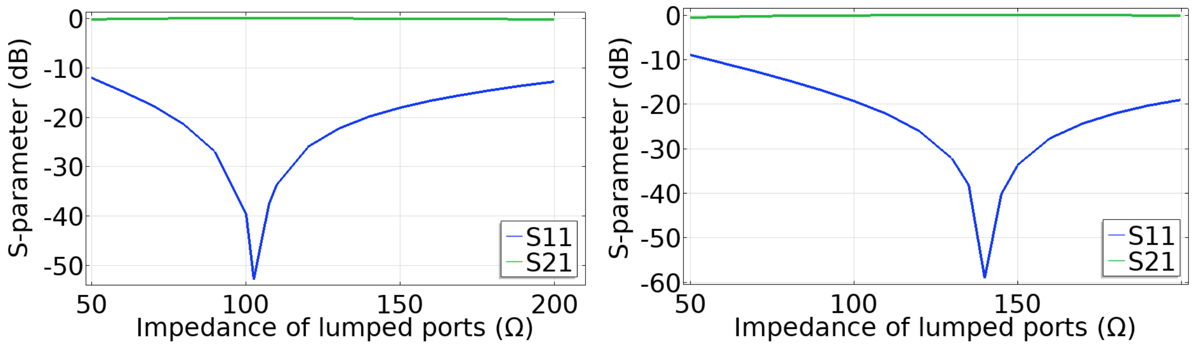

(a) Surroundings assigned as PEC.

(b) Surroundings assigned as PMC.

Figure 4.4: Simulation of S-parameters using impedance sweep of the TL input and output port in frequency domain (f=1 MHz) and for two different boundary conditions.

In the setups presented in Figure 4.3 and 4.4 frequency domain simulations were performed. For the EMP application only one single shot pulse is excited and not a continuous excitation like simulated in the frequency domain models. The continuous feed at the excitation port probably causes superposition of the signal which not will occur in the same way for a pulse excitation in time domain. Therefore these results need to be interpreted with caution.

Another finding increasing the doubt in this simulations was obtained when increasing the excitation frequency from 1 MHz to 10 MHz and 50 MHz. The indicated impedance value for best impedance value changed drastically. In the Comsol simulations, no losses are modelled. Thus the impedance of the TL should be determined by its inductance and capacitance only, parameters that are not frequency dependent. The contradictory simulation result indicate deficiencies in the simulation setup and therefore, once more, indicating that the results have to be interpreted with caution.

4.1.3 Electric field simulation of spark gap

As a part in the design of the pressurised vessel and spark gap electrodes, electric field simulations were performed. Utilising symmetry, this was modelled using a 2D axisymmetric geometry. Simulation results of electric field distribution and electric field homogeneity in the spark gap are presented in Figure 4.5. The presented geometry in Figure 4.5a, is the final design with a electrode diameter D=50 mm and a spark gap, d_{gap}=10 mm but adjustable within 0-15 mm. The gap distance was adjusted by moving (turning) the sphere electrode which is mounted on a M10 threaded bar while the semisphere electrode position was fixed. The indicated maximum field stress of 20.7 kV/mm is much higher than electric strength of ambient air, given by (2.7), which emphases the need of a vessel to increase gas pressure or use another insulating gas than air. The field uniformity in the spark gap was found to be 82 % calculated from the minimum and max values, 16.8 and 20.5 kV/mm respectively, in Figure 4.5b.

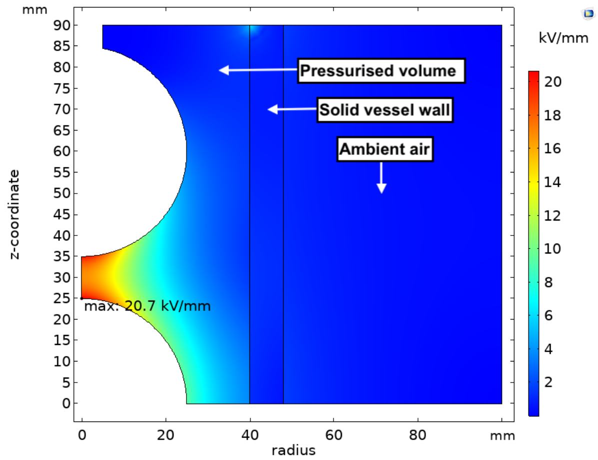

(a) Simulated electric field distribution in vicinity of spark gap.

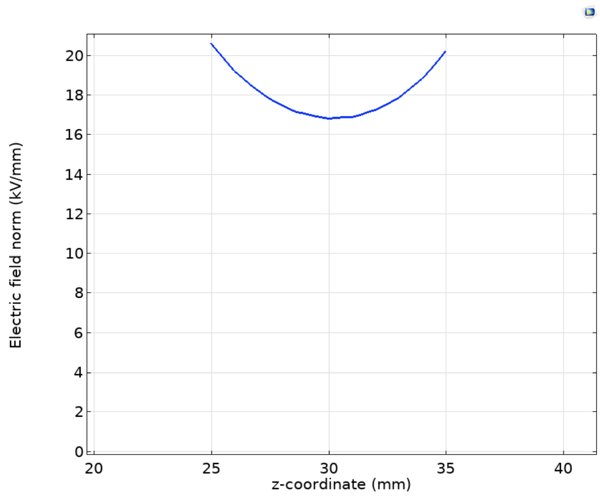

(b) Simulated electric field norm in spark gap at radius=0 mm.

Figure 4.5: Simulated electric field in spark gap with sphere to semi-sphere electrode design with an applied voltage of 180 kV and spark gap distance of 10 mm.

4.2 Final design of EMP testbed

This section presents drawings and photos of the EMP testbed. Cad drawings of the design of rapid discharge circuit are presented in Figure 4.6. The brown parts are insulating support legs. The blue part is an aluminium plate connecting the TL wires to the spark gap. The pink sheets represent insulating material: nylon and PVC. The GA capacitors visualised in grey rest on a horizontal nylon sheet which also helps increasing the clearance by prolonging the air path from the capacitor electrodes to the grounded floor, thus reducing the risk of flashover. Owing to the higher dielectric strength of solid material like PVC and Nylon compared to air the risk of breakdown in these solid materials compared to air is low. The vertical sheet is made of PVC and has internal M12 threads for fastening the nylon threaded rods holding the pressure vessel cylinder showed in light blue in place. The light green parts are nylon M12 threaded bars and nuts. The orange part represent used conducting material; brass and copper.

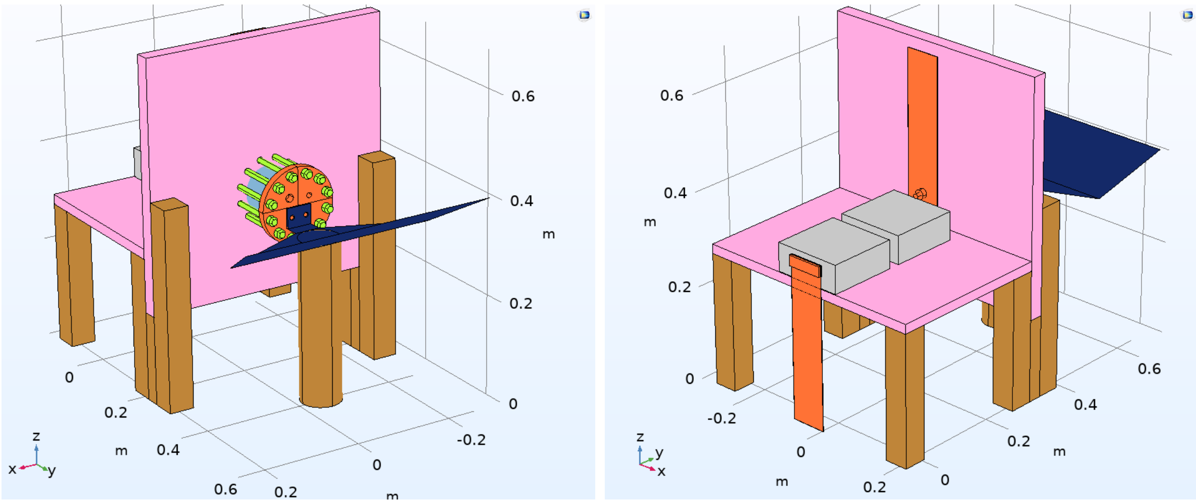

(a) View from TL side of spark gap. (b) View from GA capacitor side of spark gap.

Figure 4.6: Cad drawing of the rapid discharge circuit design.

In Figure 4.7, an overview of the complete constructed testbed is shown. The EMP generator can be seen at the bottom left corner. In the middle of each inclined section of the TL, there is a wooden support to keep the individual wires at same height and to reduce their sag. The cubic wooden frame in the middle of the TL holds up the top horizontal part of the TL. At all the intersection points of the wooden studs, fixtures were made by either sawing custom u-shaped slits forcing them in place or using nylon threaded rods and nuts. In the figure, also the additional grounding net placed under the TL can be seen.

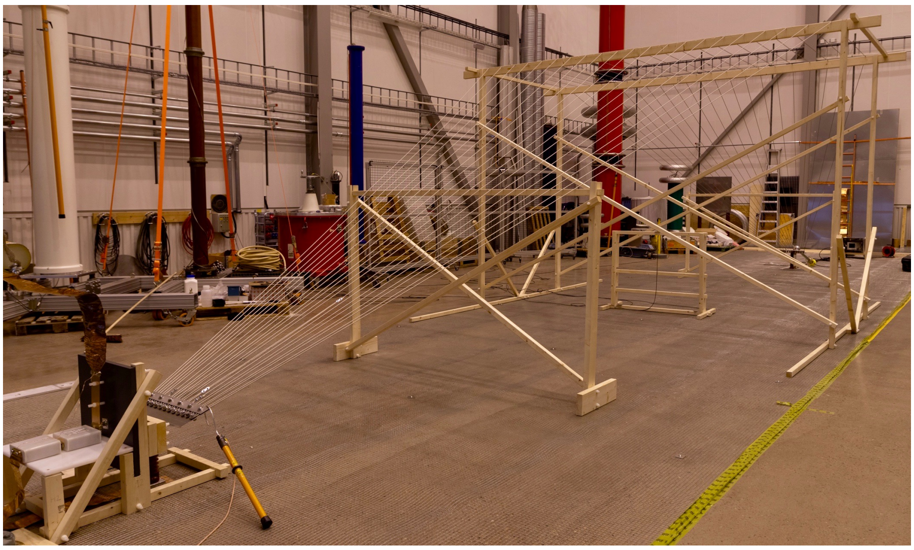

Figure 4.7: EMP testbed overview.

In Figure 4.8, the setup of the impulse charging circuit, rapid discharge circuit and HV dividers are displayed. Note that only the two lowest stages of the ASEA Marx generator visible in the background were used. The ribbon seen to the left is the tail resistor of the Marx generator and the front resistor is almost completely hidden behind the yellow support insulator. The PIKA VFT600 is here seen connection point of spark gap electrode and TL referred to as position 1.

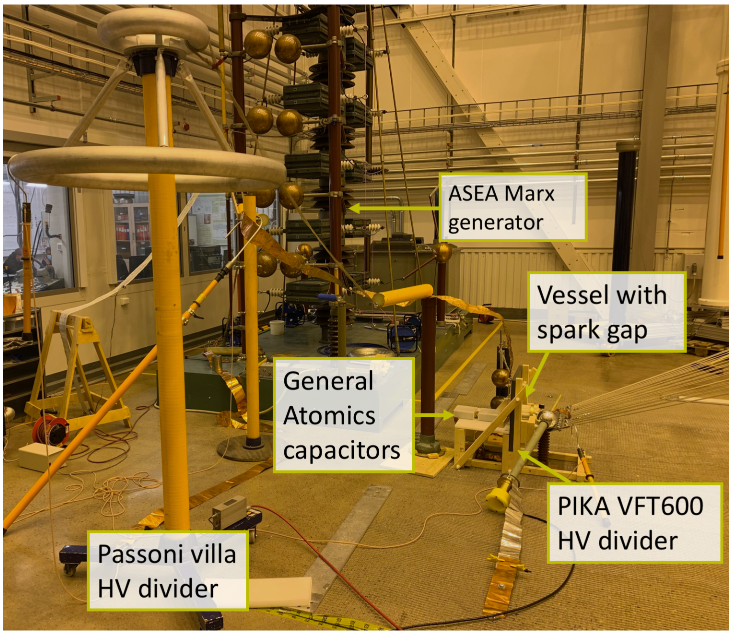

Figure 4.8: Overview of EMP generator and HV dividers

In Figure 4.9, the radiating TL is presented from two different angles. In the bottom left corner of Figure 4.9a, the rectangular aluminium plate and strap used to tension the TL wires is displayed. Here the PIKA VFT600 wire is seen connected at the water resistor end referred to as position 2 in the TL. In Figure 4.9b, a side-view of the top horizontal part of the TL is shown. The one metre high wooden stand on the floor in the middle under the TL was used for holding the field sensors in position.

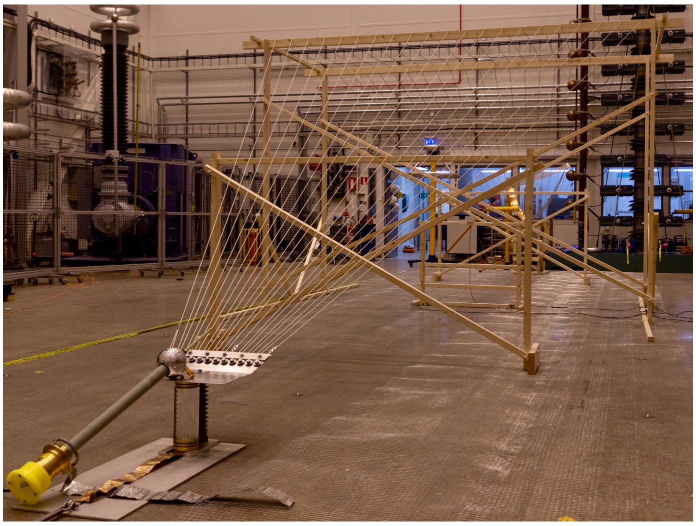

(a) View from resistor end side of TL.

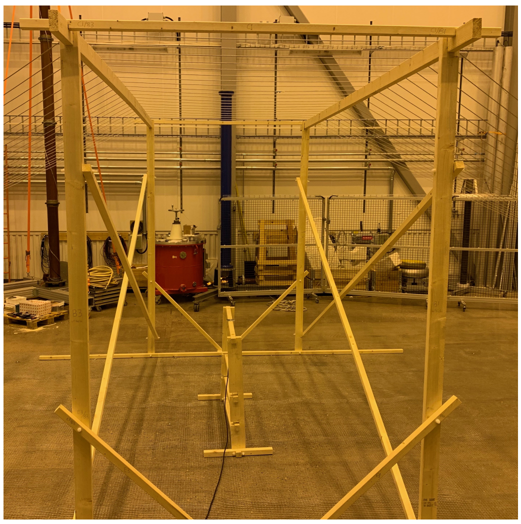

(b) Side-view of TL.

Figure 4.9: Overview of the constructed TL.

In Figure 4.10, an overview of the rapid discharge circuit is presented. The copper strip coming down from centre top is connected to ASEA marx generator. One can note that the capacitors are short circuited and grounded with a copper wire and a grounding stick is grounding the TL, which naturally only are present when the EMP testbed is not operation as a safety precaution. Also here, a supporting frame was built using wooden studs assembled by using nylon threaded bars and nuts. The TL wires are connected to the spark gap via a triangular shaped aluminium sheet that is fixed in place by a support insulator bolted to the floor.

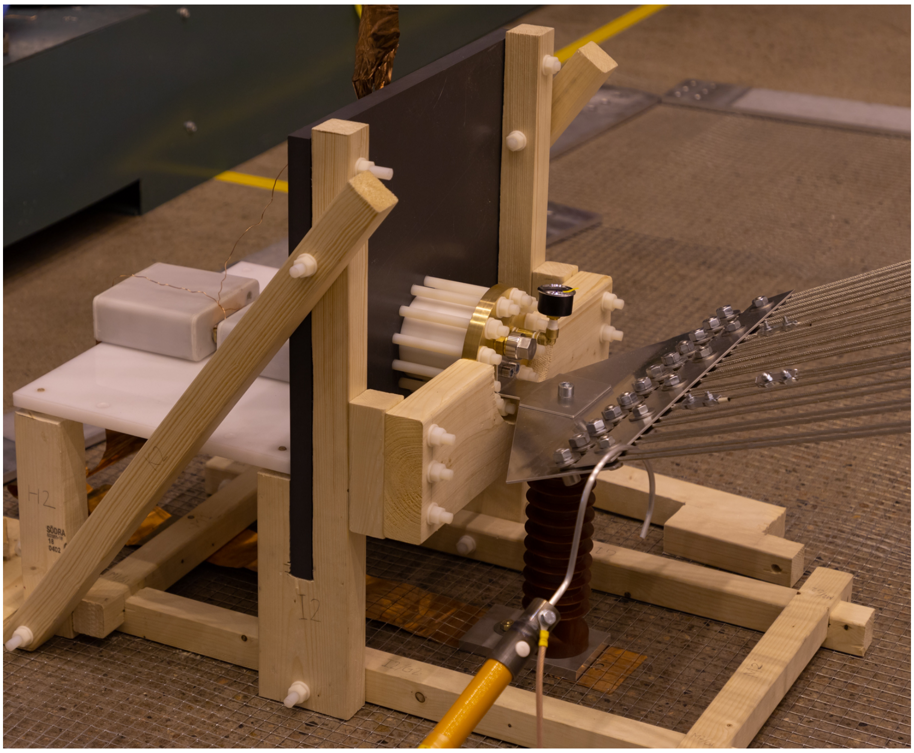

Figure 4.10: Overview of the rapid discharge circuit.

In Figure 4.11, the electrodes and vessel used for the spark gap are shown. The electrodes are made of brass. In Figure 4.11a the sphere electrode is seen mounted on a brass plate with a wider groove for partial immersion of the POM cylinder and a narrow groove for an o-ring. The same type of grooves are also made in the PVC sheet shown in Figure 4.11a. Also shown in this figure are the nylon threaded bars used to press the POM cylinder tight in between the brass disk and PVC sheet to make a pressure proof enclosure. The fully assembled vessel is displayed in Figure 4.11c. The valve to the left is for the SF6 system and to the right a manometer is installed to monitor the pressure. At the bottom of the figure, the aluminium sheet connecting the TL wires to the vessel can be seen.

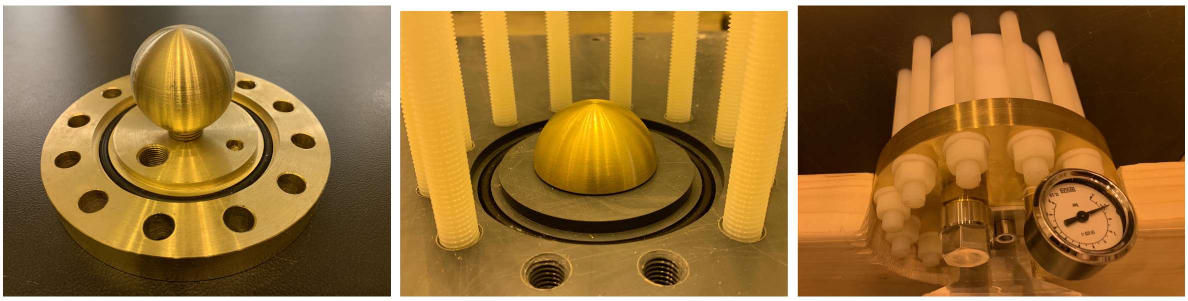

(a) Sphere electrode connected to TL side of spark gap.

(b) Semisphere electrode connected to EMP generator side of spark gap.

(c) Vessel enclosing the spark gap.

Figure 4.11: Constructed parts for the spark gap in EMP generator rapid discharge circuit.

The types of used termination resistors are presented in Figure 4.12. The three series connected wire wound resistors shown in Figure 4.12a are 25 Ω each giving a total resistance of 75 Ω. Figure 4.12b shows the water resistor, in the top right corner the PIKA VFT600 HV divider is positioned on top of a aluminium sheet connecting the TL wires to the termination resistor.

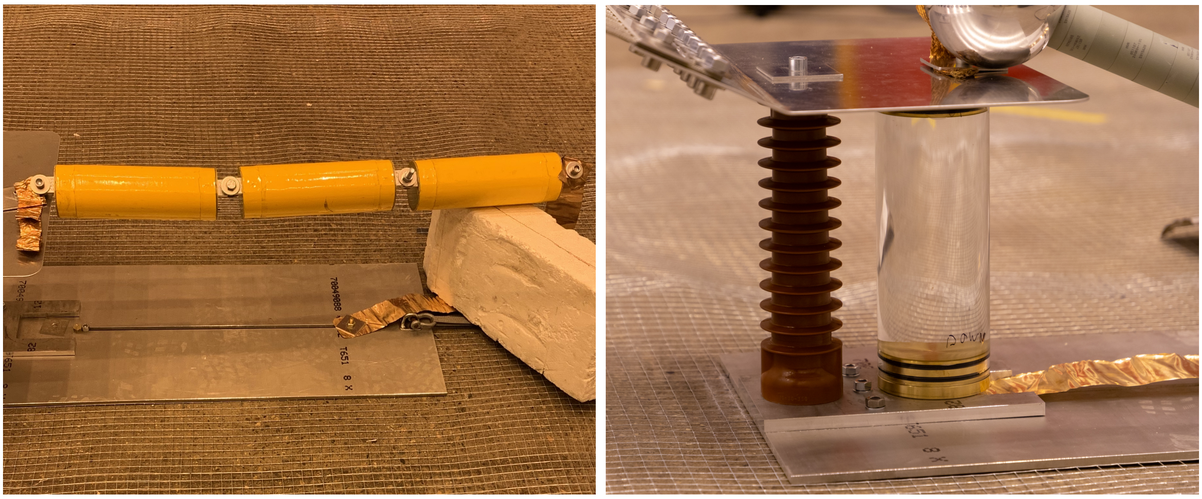

(a) Wire wound resistors. (b) Water resistor.

Figure 4.12: Termination resistors used in the TL.

4.3 Experimental results from the EMP testbed

In this section, experimental results obtained with the EMP testbed in the HV laboratory are presented. Once the setup of the testbed was complete the behaviour of the EMP generator was investigated in terms of the triggering flashover voltage and its scattering, these results are presented in section 4.3.1. The signals observed by the different measurement devices are described in detail in Section 4.3.2. The impact of different sort of terminations of the radiation system was explored in Section 4.3.3. In Section 4.3.4, the performance of the different field sensors presented in Figure 3.1 are compared. In Section 4.3.5, the signal attenuation in the TL is analysed and finally, in Section 4.3.6, field sensor measurements from different positions inside the intended test volume are compared.

4.3.1 Evaluation of EMP trigger system

There were several issues with the EMP triggering mechanism which behaved in unexpected ways. Initially the spark gap distance, d_{gap}, was set to 10 mm and with this setup, the breakdown voltage was quite inconsistent. It was suspected that the reason for the scatter in the breakdown voltage could be a too inhomogeneous electric field in the spark gap. Thus d_{gap} was reduced to 6 mm which should increase the level of homogeneity of electric field in the spark gap.

Numerical values related to spark gap triggering are presented in Table 4.1. Here p_{SF6} is the absolute pressure of SF6 in the vessel where the spark gap triggering the EMP is placed and the theoretical breakdown voltage V_{bd} is calculated from (2.7). The given charging voltage is the value of the voltage across the ASEA marx capacitors before that generator was triggered. The initial results with $p_{SF6} = 6$ bar were really promising as it entailed a flashover voltage of 173 kV which was close to the desired level of 180 kV. Furthermore the breakdown voltage was consistent as the standard deviation was only 2.73 kV which was considered low as it corresponded to less than two percent of the median value. Unfortunately though, problem with external flashovers in the EMP generator arise. Flashovers were observed visually across the GA capacitors but it was hard to tell the exact location of the discharge path. Inspection of the GA capacitor and its electrodes showed no signs of burned surface discharge paths. The discharge could have been from the incoming charging copper strip from marx generator to the grounded end of GA capacitor bank.

To generate pulses repeatedly, without external flashovers, the pressure was lowered to 1.5 bar yielding a lower value of V_{bd} and most likely a too low electric field amplitude in the TL test volume. With this setup, a significant scatter in the breakdown voltage level and the standard deviation corresponded to 13 % of the median value. A suspected reason for this increased scatter was impurities in the gas system resulting in non pure SF6 gas.

p_{SF6} [bar]	Theoretic V_{bd} [kV]	Nr of pulses	Charging voltage [kV]	Median of V_{bd} [kV]	Std dev of V_{bd} [kV]
3	160	10	232	173	2.73
1.5	80	75	180	132	17.2

Table 4.1: Measured V_{bd} for spark gap with d_{gap}=6 mm.

Presented in Figure 4.13 is the full timescale where the voltage dividers record a nonzero voltage, except what was believed to be measurement noise. First observed event is the triggering and impulse front from the ASEA marx generator. The next event to happen is the ignition of the spark gap in the secondary generator circuit and the PIKA VFT600 divider observes the EMP front.

When the vessel spark gap was conducting, the Passoni Villa and PIKA VFT600 HV dividers essentially measured the same point in the circuit meaning should have observed the same voltage level as long as the spark gap remained conducting and then if extinguishing, the Passoni Villa should observe the voltage across the GA capacitors as these were discharged through ASEA marx generator's front and tail resistor and the PIKA VFT600 should observe the voltage in the TL including eventual reflections. However, as can be seen in Figure 4.13, the voltage dividers measured the same voltage level all throughout the whole discharge of the ASEA Marx generator from ≈ 0.5 μs where the voltage is about 75 kV until it reduced to zero after ≈ 48 μs. This was most likely caused by the implications of the remaining charge in primary generator circuit when the secondary generator circuit was triggered. This fact suggest that the spark gap remained conducting even after the energy in GA capacitors were discharged into the TL, in contrast to extinguish and become insulating much faster as was both desired and expected when using SF6 which has high electron affinity yielding good possibilities for arc extinguishing.

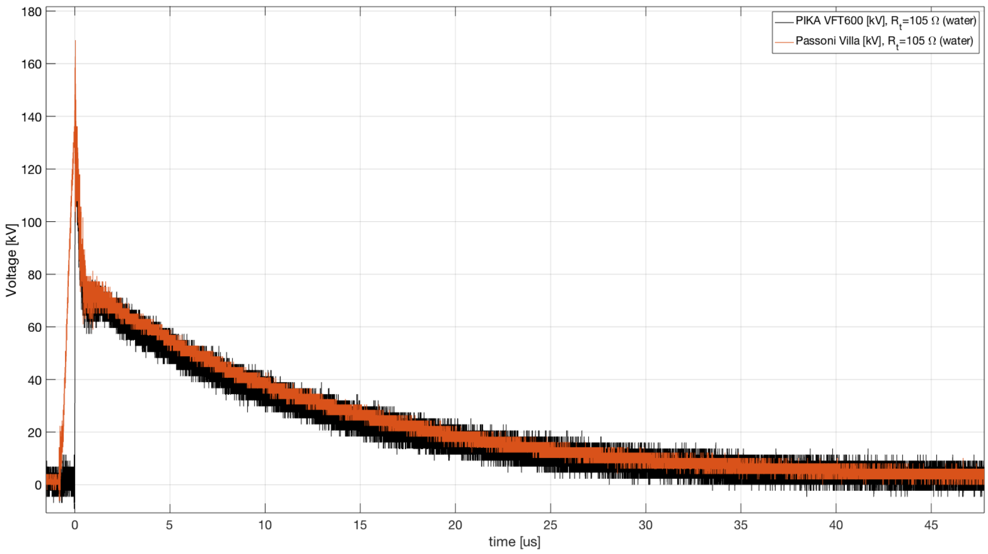

Figure 4.13: Voltage measurements indicating impulse charging, EMP trigger and capacitor discharge events in the EMP generator.

4.3.2 Acquired measurements in the EMP testbed

As described in Section 3.5.1, three main quantities were measured when generating EMPs, these measurements are displayed in Figure 4.14. The TL was terminated with a 105 Ω water resistor in these measurements. The time sync of the oscilloscope trigger was set so that the ignition of the spark gap inside SF6 vessel occurs at t_0. This event was preceded by the ignition of the spark gap in ASEA Marx generator which happened 720 ns earlier, i.e. when Passoni Villa HV divider started to observe an increased voltage as seen in Figure 4.14a. The measured signal from the D-dot sensor, at time-point just after the ASEA generator was triggered, shows an oscillatory behaviour probably caused by an airborne EM signal from the ASEA marx generator's spark gap. The full unchopped pulse from the ASEA Marx had a rise time of 900 ns, with time to chopping of 720 ns it was front chopped. The Passoni Villa HV divider recorded the output voltage of ASEA Marx generator which means it measured the voltage across the General Atomic capacitors, hence also the voltage stress applied on the spark gap inside the SF6 vessel before ignition. The ASEA Marx generator trigger system consists of a spark plug placed at the spark gap in the lowest stage. About 30 ns after the ASEA Marx generator was triggered, the D-dot sensor started to observe an oscillatory signal. A 30 ns time delay corresponds to a distance of 9 m for a EM wave propagating in air which agrees well with the actual distance from the ASEA Marx's spark gap to the D-dot sensor location in the laboratory. This verifies that the triggering of the ASEA Marx generator most likely emitted an EM pulse observed as airborne noise. These oscillation were still ongoing when the D-dot sensor observed the EMP of interest which caused superposition of the signals.

Figure 4.14b presents a zoomed in view of the ignition of the spark gap inside SF6 vessel. As the voltage stress reached 120 kV the spark gap breaks down and the PIKA VFT600 observed the EMP as the GA capacitors were discharged into the TL. After ignition of the vessel spark gap ignition, the signal measured by Passoni Villa HV divider started to show an unexpected oscillatory behaviour resulting in peaks of 146 kV. However these measured points above 120 kV most likely were an artifact from the Passoni Villa

HV divider itself which would invalidate these data points. The reason for believing so is that that Passoni Villa divider is not designed to observe fast transients in nanosecond range. The PIKA VFT600 divider has better performance at these fast transients and recorded a maximum voltage of 124 kV for the present pulse.

As discussed in Section 4.3.1, it seemed that the vessel spark gap remained conductive even after the GA capacitors had discharged the energy of the intended EMP. The measured voltages from Passoni Villa and PIKA VFT600 follows each other very closely from t=30 ns and onward. A consequent of the spark gap remaining conductive is that the ASEA Marx generator continues to discharge into TL extending the duration of the pulse significantly. Thus the FWHM of the pulse from the GA capacitor discharge could not be measured as it was masked by the discharge of the ASEA Marx capacitors.

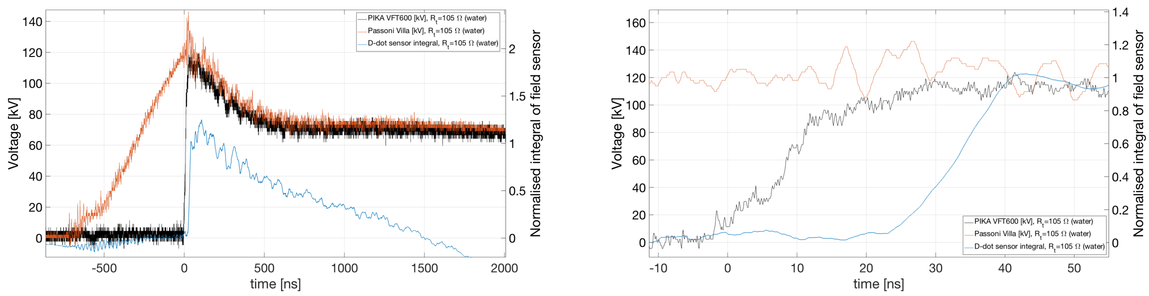

(a) Comprehensive timescale. (b) Zoomed in timescale of the EMP front.

Figure 4.14: Example of measurement data acquired to verify EMP testbed performance.

4.3.3 Measured impact of TL termination resistor

Figure 4.15 presents measurements from the EMP testbed with three different TL termination resistors. The PIKA VFT600 was placed at TL resistor termination end.

When using only the 4 kΩ HV divider as termination, significant reflections seems to have occurred. The measurement signal was clipped as the operating range of oscilloscope was exceeded. For this pulse, external flashover across the GA capacitors was observed visually. One possible explanation to observed phenomenon is that first, reflection at the termination end occurred and when this reflecting pulse returned to the spark gap the voltage superposition resulted in so high voltage stress across GA capacitors that a flashover occured. A 216 ns time delay between oscillation peaks was measured which corresponds to a wave travelling 65 m in air (32.5 m single way to a reflection point) or a slightly longer distance in travelling in cables. No such distances through air were present. One possible cause of the oscillations are events related to the flashover to ground.

Measurements with a 75 Ω wire wounded termination resistor also showed significant oscillations. A 190 ns time delay between peaks of the measured signals with wire wound termination resistors correspond to a wave travelling 58 m through air (29 m single way to a reflection point) or a slightly longer distance in travelling in cables. The length of the wires inside the used resistor was unknown. Even if it can not be determined with certainty, a likely explanation is that the frequency of the oscillation is related to internal length of the wire wounded resistors.

Measurements with the water resistors showed small oscillations not as prominent as in the two other cases. A water resistor was therefore preferred as its low-inductance prevented occurrence of oscillations.

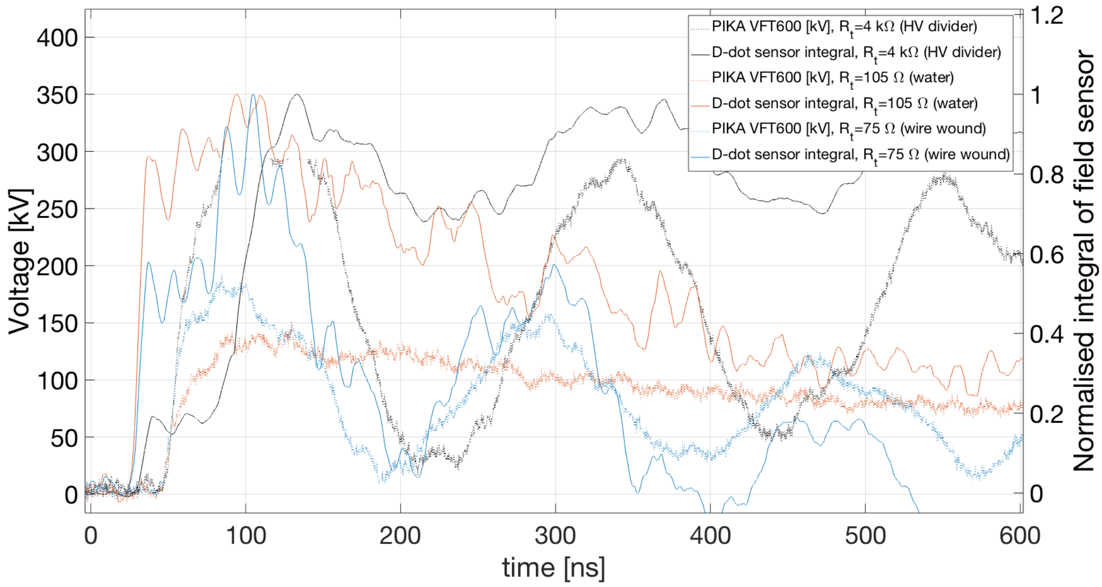

Figure 4.15: Measurements with different TL termination resistor types; water resistor, wire wound resistor and high ohmic HV divider only.

Due to difficulties in determining TL characteristic impedance with certainty from simulations in Section 4.1.2, different resistance values of the terminating water resistor were tried experimentally to obtain a properly matched TL termination. Resistance adjustment of the water resistor was easily done by mixing sodium carbonate into the water.

Figure 4.16 presents measurements from the comparison of various resistance values of water termination resistor. The measurement signal obtained from the D-dot sensor was normalised with respect to the first amplitude peak of respective pulse.

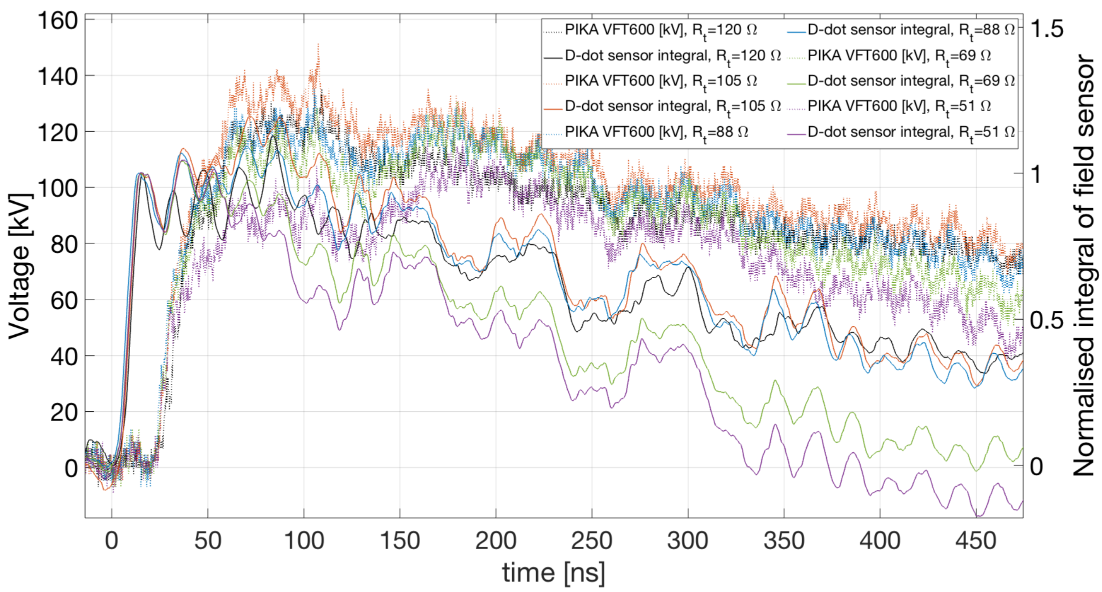

Figure 4.16: Measured voltage at TL termination and electric field in intended test volume for different resistance values of terminating water resistor.

All the measurements shown in Figure 4.16 have been time synced so that the D-dot field sensor observation of the start of the EMP front occurs at t_0.From the time-point when the D-dot sensor observes the initial EMP to the first eventual reflection at the termination arrives to the D-dot sensor, the pulse needs to travel 14 m along the TL corresponding to 47 ns. However, no reflections of corresponding time were observed indicating well-made impedance matching for the explored resistance values. Termination resistance variation appear to have influenced discharge time of the capacitor in the generator circuit though. Looking at t=450 ns, the measured voltage was 80 kV for $R_t = 120\ \Omega$ compared to 50 kV for $R_t = 51\ \Omega$.

4.3.4 Evaluation of field sensors

By the means that not all parts in the measurement system were calibrated in a traceable way, a complete verification of the testbed measurement system could not be done. This evaluation should therefore be considered as an indication of the functionality of the testbed rather than a complete verification of ”RS105” compliance that would be required for performing customer test services.

Various types of cables were tried for the field sensor to see how these affected the measure signal. Initially the signal from the D-dot field sensor was transferred via coaxial RG58 cables of ca 42 m from the HV laboratory into the control room where the oscilloscope was placed. It was not possible to detect the EMP with the D-dot sensor using this setup, a likely explanation could be that the signal attenuates too much in these long cables. To be able too use shorter cables the oscilloscope was instead place inside the HV laboratory inside a shielded and grounded rack to protect it from EMP exposure. Different types of cable with BNC connectors was tried including 10 m long standard RG58, 5 m long double shielded RG58 and 13 m long *Bellden Triax* (double shielded). It was not possible to detect the EMP with any of these cables as the obtained signals had too much noise. The use of shorter cables is still believed to be an improvement as the signal attenuation is reduced. Interference test of the cables was performed by removing the D-dot field sensor and instead short circuiting the cable end which theoretically should give a signal of 0 volt. The obtained results was however very similar to the case when a D-dot sensor was connected which indicates that the quality of the cable’s shielding is insufficient. These findings indicates that cables with high quality shielding are required. When trying a 10 m long *Megaphase Warrior cable* the noise was significantly suppressed and the EMP could be detected.

Figure 4.17 presents a comparison of the performance of the two D-dot sensors and the B-dot sensors (displayed in Figure 3.1) used. One sensor was tested at time as only one copy of properly shielded measurement cable for this purpose was available. As the signals from the two HV dividers were similar for the three pulses a straightforward comparison of the field sensor is believed to be valid. All three sensors showed similar EMP front time. The amplitude of the B-dot and BNC type D-dot are similar while the N-type sensor gave a pulse with three times higher amplitude than the others. This indicates that the N-type D-dot sensor is more sensitive. However it also showed more distinct distortions on the signal looking at timescale from 60 to 100 ns.

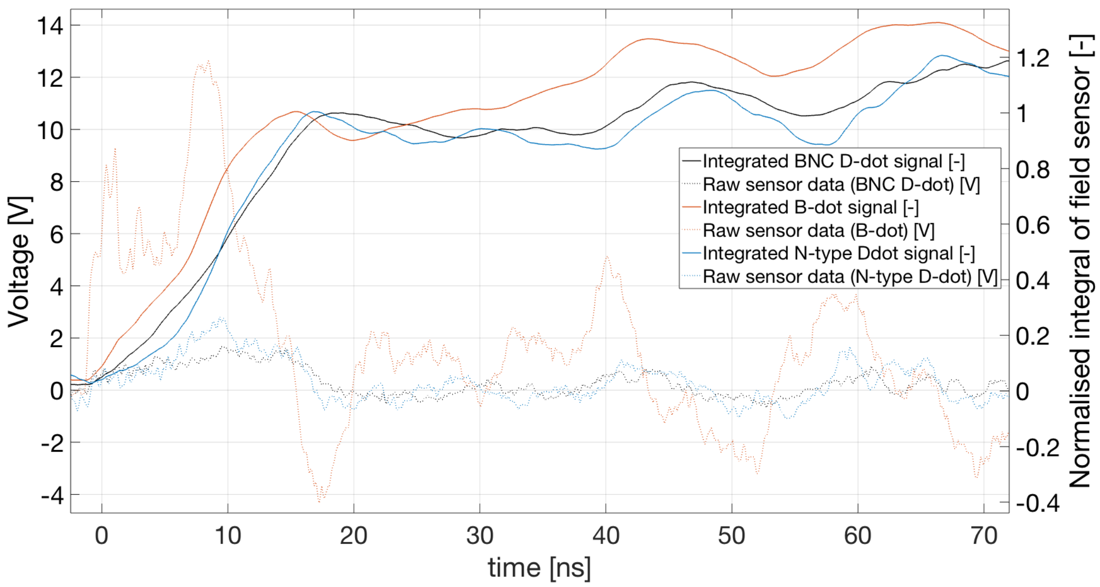

Figure 4.17: EMP measured with the three different field sensors displayed in Figure 3.1.

In Table 4.2 selected parameters from the measurement data from the field sensors are presented. Here, V_{bd} was measured with Passoni Villa HV divider and is included to indicate that there were amplitude differences in the emitted pulses.

Field sensor description	Measured front time [ns]	Measured V_{bd} [kV]	Measured A_i/A_1
D-dot (BNC contact)	13.5	124	1
B-dot	13.3	116	5.3
D-dot (N-type contact)	11.1	124	1.14

Table 4.2: Numerical values from the comparison of the field sensors.

4.3.5 Measured pulse attenuation and distortion in the TL

Figure 4.18 presents the results of two pulses where the difference in the acquisition of these pulses was the positioning of the PIKA VFT600 where the spark gap end of the TL is referred to position 1 and in opposite end of the TL, in parallel with termination resistor R_t is referred to as position 2. The measurement curves from the Passoni Villa HV divider and the D-dot sensor for the two pulses displayed, are well overlapped meaning that the generated EMP was similar in both cases which makes a direct comparison of the measurement curves from PIKA VFT600 valid. The measured signals from the D-dot sensor for the two pulses are time synced such that the field sensor observes the start of the EMP front at t_0.

Looking at the measurements from PIKA VFT600 at position 2, the PIKA VFT600 observed the pulse ≈23 ns before the D-dot sensor. Naturally, the order is opposite for the setup with PIKA VFT600 at position 1 the PIKA VFT600 observes the pulse ≈23 ns after the D-dot sensor. The path along the TL from end to end was 14 m giving a distance of 7 m from respective end to the centre point where the D-dot sensor was placed. At the speed of light, the pulse travels a distance of 7 m in 23.3 ns which matches well to the measured time delay between measurement devices.

The voltage across the GA capacitors just before spark gap ignition was 142 kV and the setup with PIKA VFT600, at position 1, was expected to give similar amplitude values. However a peak of 117 kV with a rise time of 8 ns is observed. Eventually though, a voltage reading of 144 kV with a corresponding rise time of 25 ns is observed. The succeeding voltage increase after the first peak of 117 kV could have been caused by reflections due to impedance mismatching in the EMP generator circuit. For the measurements acquired with the PIKA VFT600 at position 2, the first peak was 58 kV but the voltage level eventually increased to 99 kV. No matter if considering the first peak or the eventual maximum voltage value, the results indicate that there are significant losses in the TL. A comparison of the measured pulse shape by PIKA VFT600 at position 2 with measurement at position 1 indicate that the pulse also seem to has been distorted by the TL.

From the D-dot sensor measurements, a front time of 8 ns was obtained. Some oscillations in the D-dot sensor signal can be observed as well. It had a period time of 19 ns which, if caused by reflections from surrounding objects, corresponds to a wave propagation distance in air of 5.7 metre. The TL itself was much longer (14 m), indicating that this ringing was not caused by impedance mismatching at TL ends.

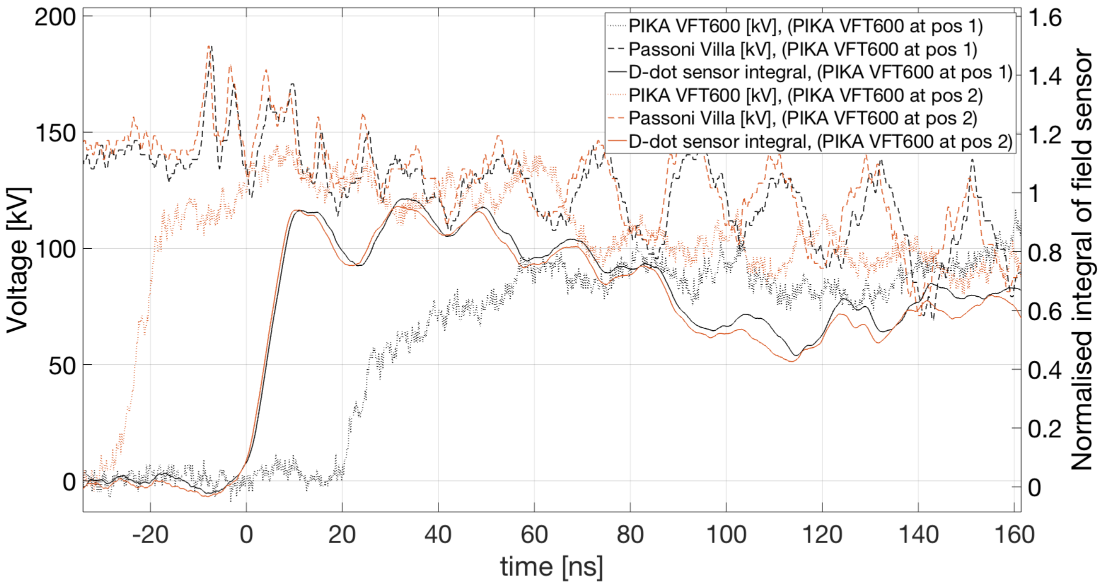

Figure 4.18: EMP measured with HV dividers at both ends of the TL to evaluate signal attenuation and distortion. $R_t = 50\ \Omega$ water resistor.

Another investigation of the EMP amplitude attenuation when propagating along the TL is presented in Figure 4.19. The D-dot sensor was moved along the centre line of TL (moving in y-direction along x=0) and measurements were taken at 7 positions. Here, d is the distance from spark gap end of the TL to the field sensor positioned at a height of 1 m above ground floor for all 7 positions. The timescale of the plot has been synced so the spark gap ignition for respective pulse occurs at t=0 s, yielding time-point of pulse front start varies from t=14 ns to t=37 ns depending on sensor position as it takes longer time for the EMP to travel to sensor positions further distanced from the spark gap.

The total length of the TL was 13.2 m in horizontal direction from end to end, but the shortest path along the TL wires was 14 m from end to end. At each position, five EMP pulses was generated to get representative results. The integrated signals from the D-dot sensor were amplitude normalised to the first occurring peak. The reason for the pulse amplitude exceeding one, see data within 60 to 80 ns on the timescale, is believed to be due to succeeding oscillations caused by reflections from laboratory walls and surrounding grounded laboratory equipment. Looking at the plot for position where $d = 4$ m, the period time of the oscillation is 15 ns which would correspond to a wave propagation of 5 metre which implicates a one way distance of 2.5 metre from the TL to the reflection point.

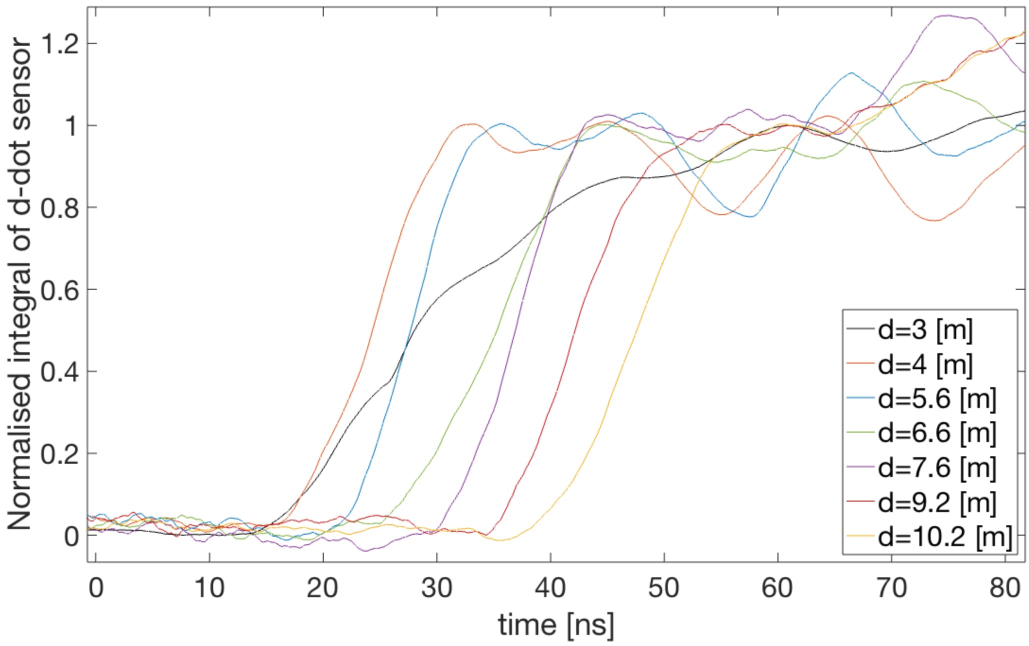

Figure 4.19: Comparison of EMP pulse shape measured at different field sensor positions along TL.

In Table 4.3, numerical values from measurements plotted in Figure 4.19 are presented together with expected theoretical values. Here, h_a is the TL height at respective D-dot sensor position. Given the values of V_{bd} and h_a for the pulses to be compared, it would be reasonable to also see the same variations in the amplitude of the D-dot sensor signal. The amplitude of the integrated D-dot sensor signal is denoted as A with subscript i referring to the value of d to tell the pulses apart. Both theoretic amplitude values and measured values are compared with respect to the corresponding values for $d = 6.6$ m which is the intended place for the EUT in the testbed. The table also presents the measured front times. Both the measured amplitude and front time stand out considerably for sensor position at $d = 3$ m. Measurement artifact of the field sensor is a possible explanation as the measured values stand out in an unreasonable way. A possible reason could be imperfect field sensor design yielding a maximum field intensity capability. The mean of the front time measured for the other six pulses was 11.3 ns, where the spread is also quite significant indicating limited repeatability of the generated EMPs.

d [m]	h_a [m]	V_{bd} [kV]	Theoretic $A_i/A_{6.6}$	Measured $A_i/A_{6.6}$	Measured A_i/ Teoretic A_i	Front time [ns]
3	1.7	126	1,79	5.02	2.80	34.6
4	2.2	124	1,36	1.64	1.21	11.1
5.6	3	124	1	1.12	1.12	8.8
6.6	3	124	1	1	1	13.4
7.6	3	114	0.92	0.88	0.96	9.7
9.2	2.2	132	1.45	1.31	0.90	11.7
10.2	1.7	122	1.76	1.52	0.86	13

Table 4.3: Numerical results from D-dot sensor signal acquired at different positions along TL.

4.3.6 Evaluation of electric field distribution in the intended test volume

The D-dot sensor was placed in five different sensor positions under the TL, all at the same distance of 6.6 m from the spark gap where the EUT is intended to be placed. As instructed in the "RS105" test standard, this preparation procedure should be done to evaluate the field uniformity inside the intended test volume.

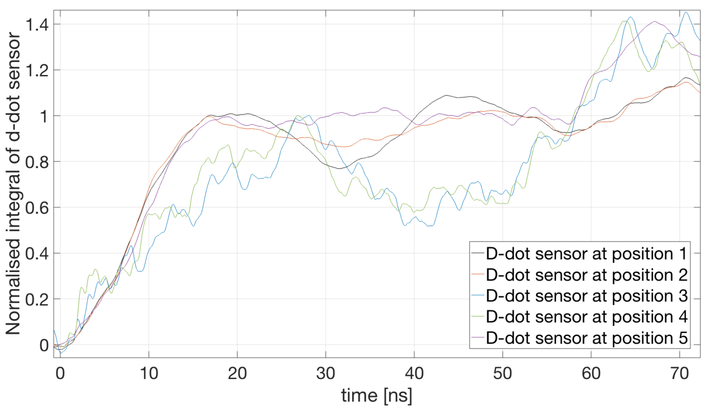

(a) Normalised integral of D-dot sensor data.

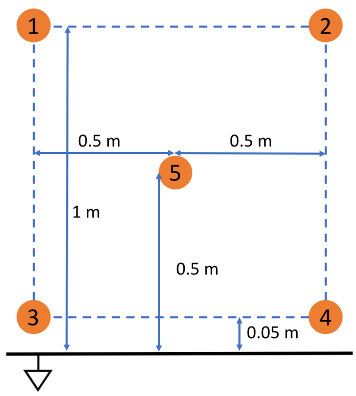

(b) The five sensor positions in xz-plane, pos 5 at x=0.

Figure 4.20: Results from field sensor measurements at five positions as described in a verification procedure in "RS105" test standards

Table 4.4 presents numerical results related to the plots in Figure 4.20. The measured signal amplitudes have been normalised with respect to the measurement from position 3 for comparison. The results shown in Table 4.20 are unexpected as, rather than indicating a homogeneous field as expected from simulations, the vertical position of the sensor strongly influenced the measured signal amplitude. It should be remembered that basic type and not calibrated field sensors are used and that it is unknown if the measured differences in signal amplitude is trustworthy or if caused by characteristics of inadequate field sensor. The presence of the D-dot sensor itself might also have influenced the field distribution as the 3x70x70 mm aluminium plate was grounded via the measurement cable to the grounded oscilloscope. Moreover, the variation in the measured pulse front time is neither reasonable which further suggests limitation in the field sensor performance.

D-dot sensor position	V_{bd} [kV]	Measured A_i/A_3	Measured front time [ns]
1	136	7.8	11
2	134	7.7	10.7
3	134	1	23
4	142	1.1	22.2
5	136	3.8	12.2

Table 4.4: Numerical values from measurement for five D-dot sensor positions according to testbed verification procedure described in ”RS105” test standard.

4.4 Future work and suggested testbed improvements

Experimental results revealed that not all requirements of ”RS105” test standard was fulfilled. This section suggests several testbed improvements to meet these requirements.

4.4.1 Replacing impulse charging with DC charging

The impulse charging circuit was found to entail several unfavourable characteristics, i.e. its triggering system emitted EM pulses detectable by the D-dot sensor and the vessel spark gap remained conducting throughout the discharge process of the impulse generator. To evade these problems, the impulse charging circuit (see Figure 2.2) could be replaced with a DC charging circuit as presented in Figure 4.21 where a DC charging circuit is highlighted in green, a rapid discharge circuit in blue and the radiating transmission line with termination resistors in red. With this setup, the GA capacitors are the only capacitors to be discharged at moment of emitting an EMP which should be a beneficial factor in terms of reducing pulse width. A DC generator, V_{DC}, is introduced to charge the GA capacitors via a current limiting resistor R_{DC} which also protects the DC generator by blocking eventual transients from spark gap ignition to be fed back to the DC generator.

The resistor R_{DC} should be high ohmic to prevent the DC generator to recharge C_{GA} to quickly after the spark gap have ignited to give the spark gap enough time to become insulating and once again increase vessel pressure. Eventual need of an (automatic) galvanic disconnector between the DC generator and GA capacitor just after emitting an EMP should also be investigated. Alternatively, a control system automatically putting the DC generator output to ground potential after emitting an EMP could be used.

Commercial available DC generator should be explored. A key criterion is output voltage capability up to 200 kV. Another option is to construct a DC generator in-house. One solution for doing so, is to use a commercial one phase AC variac transformer, an in-house made AC step-up transformer and an in-house constructed Cockcroft-Walton generator (CW generator). The idea is to connect the AC variac transformer input to the mains and its output to a step-up AC transformer with a secondary winding voltage rating in the range of a few kV. A CW generator, which each internal stage of a few kV, can then be used to rectify the stepped up AC voltage to DC voltage. The CW generator should be configured with the number of stages needed to provide an output DC voltage up to 200 kV.

As DC charging is much slower than impulse charging there might be an increased risk of flashover at GA capacitors as an eventual discharge channels have more time to develop. Suggested preventive action is to overview, and if possible increase, the clearance between incoming charging strip and GA capacitors grounding strip. An additional action to consider to eliminate the clearance issue is to immerse the GA capacitors completely in a liquid that has higher dielectric strength than air such as oil. The motivation of this action is to evade problems of external flashovers in the generator circuit and thereby enable reliable operation at higher voltage levels.

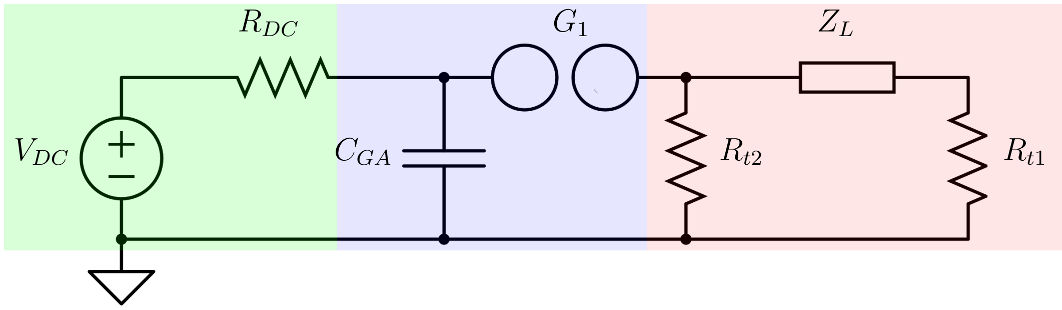

Figure 4.21: Suggested circuit diagram of improved EMP testbed with DC charging.

The presence of an additional resistor R_{t2} should be noted in Figure 4.21. In the setup of the circuit R_{t2} acts like a tail resistor to the impulse generator consisting of C_{GA} and G_1 and could therefore affect the tail time of the generated EMP. In the EMP generator setup with an impulse charging circuit, the front and tail resistors of the primary generator circuit also served as tail resistor for the secondary generator circuit. An investigation of whether the resistor R_{t2} is needed or not have to be performed. Furthermore, assigning $R_{t2} = Z_L$ suppresses eventual reflections from impedance mismatching.

4.4.2 SF6 free spark gap trigger system

From experience, operating the SF6 system was time consuming and gas leakages, even though very small, was inevitable. Thus, there are both practical and environmental reasons to not use SF6. For DC charging, the most promising trigger system of the ones presented in Section 2.1.3 is to trigger by decreasing air pressure in vessel. This is argued by a simple setup with no moving parts nor extra parts that would need to be installed inside the pressure vessel.

4.4.3 Non-reflective test environment

Oscillations observed in the measurement signals were likely, at least partly, caused by reflections from HV laboratory walls and ceiling. This motivates to find new premises for the testbed. Moving to a portable source for DC charging obviates the dependency of using the immobile impulse marx generator in the HV laboratory. Suggested future testsite is either outdoors at a flat parking lot or inside an anechoic chamber.

4.4.4 Procurement of measurement cables and field sensors

Properly shielded measurement cables for the field sensor showed to be critical to achieve useful measurement data. It is suggested to invest in cables, such as Ecoflex 10 plus, dedicated for the EMP testbed. Furthermore, the home-made D-dot sensors were inadequate for test services as they are not calibrated and gave dubious measurement data.

To achieve adequate functionality of the home-made sensors, considerable time for development work would be needed. Instead, it is suggested to overview commercial available sensors and consider procurement of a D-dot sensor compliant to given specifications in "RS105" test standard.

4.4.5 Data visualisation software

Data acquisition and post-processing was time-consuming as it included several manual actions. A Labview software could be developed to make data management more efficient.

5
Conclusion

An EMP testbed for radiated susceptibility testing was designed and constructed at RISE HV laboratory. Its basic functionality was proven in terms of possibility to generate HV impulses and guiding them via a radiation system emitting en EM field. Designed and constructed parts in this project included a transmission line, vessel with a spark gap, water resistor and electric field sensors.

A Marx generator was used to generate a voltage pulse with a front time of 900 ns serving as a charging circuit for a 200 kV, 4 nF, low inductance, rapid discharge capacitor bank used for temporary storage of EMP energy. EMPs were generated by discharging these capacitors into a radiation system via a spark gap enclosed in vessel pressurised with up to 3 bar SF6 gas. The vessel spark gap breakdown voltage was set such that output pulse of the Marx generator was front chopped and thereby, automatically triggering the vessel spark gap. EMPs with a front time of 8 ns was successfully generated. Efforts were made to make the testbed compliant to test standard *MIL-STD-461G RS105* which was not achieved however as, for instance, EMP front time criteria was not fulfilled.

The radiation system consisted of 21 conducting wires forming a parallel plate structured TL that was used to guide the EMPs over the intended test volume. The constructed TL was four metre wide and three metre high and designed for test objects sized up to 1x1x1 m^3. FEM based simulations showed promising field homogeneity in the intended test object volume in the TL. A properly matched termination of the TL to ground was achieved using a water resistor.

Furthermore, D-dot sensors were fabricated and proved capable of capturing the EMP waveform in most cases. To provide absolute amplitude values the sensors need to be calibrated. Simulations of electric field distribution showed that to obtain a homogeneous field with desired amplitude of minimum 50 kV/m the TL voltage would need to be 180 kV. EMPs with an amplitude of 173 kV was successfully generated occasionally. The amplitude of reliably generated repeatable pulses was 132 kV as there were issues with external flashovers in the EMP generator circuit.

Bibliography

[1] T. Hurtig, S. Linder, K. Wiklundh, K. Fors, and S. E. Nyholm, “Introduktion till avsiktliga elektromagnetiska hot mot samhällsviktig verksamhet och kritisk infrastruktur”, FOI, Stockholm, Sweden, MSB1180, 2018. [Online]. Available: `https://www.msb.se/siteassets/dokument/amnesomraden/informationssakerhet-cybersakerhet-och-sakra-kommunikationer/utbildningsmaterial-elektromagnetiska-hot/introduktion-till-avsiktliga-elektromagnetiska-hot-mot-samhallsviktig-verksamhet-och-kritisk-infrastruktu.pdf`, Accessed on: Nov 25, 2020.

[2] RISE, ”Industrialisation and quality assurance”, n.d. [Online]. Available: `https://www.ri.se/en/about-rise/our-purpose/industrialisation-and-quality-assurance`, Accessed on: Nov 25, 2020.

[3] ”MIL-STD-461”, in *Wikipedia,* n.d. [Online]. Available: `https://en.wikipedia.org/wiki/MIL-STD-461`, Accessed on: March 23, 2021.

[4] *Electromagnetic compatibility (EMC) – Part 4-25: Testing and measurement techniques – HEMP immunity test methods for equipment and systems,* SS-EN 61000-4-25/A2, SEK Svensk Elstandard, Kista, Sweden, 2020.

[5] *Requirements for the control of electromagnetic interference characteristics of subsystems and equipment,* MIL-STD-461G, United states Department of Defence, USA, 2015.

[6] M. Magdowski and R. Vick, “Estimation of the mathematical parameters of double-exponential pulses using the nelder–mead algorithm”, *IEEE Transactions on Electromagnetic Compability*, vol. 52, no. 4, Nov. 2010.

[7] A. Küchler, *High Voltage Engineering,* Berlin: Springer vieweg, 2018.

[8] Z. Popović and B. D. Popović, *Introductory electromagnetics,* Colorado, USA: University of Colorado Boulder, 2000. [Online]. Available: `http://ecee.colorado.edu/ecen3400/ECEE_3400_Textbook.html`, Accessed on: April 9, 2021.

[9] *Insulation co-ordination - Part 1: Definitions, principles and rules,* IEC 60071-1:2019, IEC, 2006.

[10] K. Korytchenko *et al.*, “Numerical simulation of gap length influence on energy deposition in spark discharge,” *Electrical Engineering and Electromechanics*, no. 1, pp. 35–43, Feb. 2021. DOI: `10.20998/2074-272X.2021.1.06`.

[11] D. H. Staelin, *Electromagnetics and applications,* Cambridge, USA: Massachusetts Institute of Technology, 2011. [Online]. Available: `https://ocw.mit.edu/courses/electrical-engineering-and-computer-science/6-013-electromagnetics-and-applications-spring-2009/readings/MIT6_013S09_notes.pdf`, Accessed on: April 9, 2021.

[12] I. J. Bahl and D. K. Trivedi, “A designer’s guide to microstrip line”, *Microwaves*, vol. 16, pp. 174–182, May 1977.

[13] C. E. Smith and R.-S. Chang, "Microstrip transmission line with finite-width, dielectric and ground plane", *IEEE Transactions on Microwave Theory and Techniques*, vol. MTT-33, no. 9, Sep. 1985.
[14] D. M. Pozar, *Microwave engineering*, 4th ed. USA: John Wiley & Sons, Inc., 2012.
[15] *Conductance data for commonly used chemicals,* Irvine, USA, Emerson, n.d. [Online]. Available: `https://www.emerson.com/documents/automation/manual-conductance-data-for-commonly-used-chemicals-rosemount-en-68896.pdf`, Accessed on: Mars 26, 2021.
[16] J. V. Klüss and P. Hyvönen, "Practical e-field sensors for emp testing", in *2014 ICHVE International Conference on High Voltage Engineering and Application*, 2014, pp. 1–4. DOI: `10.1109/ICHVE.2014.7035413`.
[17] G. Zhang, W. Li, L. Qi, J. Liu, Z. Song, and J. Wang, "Design of wideband ghz electric field sensor integrated with optical fiber transmission link for electromagnetic pulse signal measurement", *Sensors*, vol. 18, no. 9, 2018. DOI: `10.3390/s18093167`.
[18] *Open tem cells ease emc testing of large devices* , USA: Atmel, 2003. [Online]. Available: `https://s1.dtsheet.com/store/data/001830698.pdf?key=7d8c0325c25779f0893a94a33b533980&r=1`, Accessed on: Nov 26, 2020.
[19] D. K. Cheng, *Field wave and electromagnetics*, 2nd ed. Harlow, UK: Pearson Education Limited, 2014.
[20] *Striplines and tem-cells: Relation between cut-off frequency and height under the plate*, Switzerland: Montena, n.d. [Online]. Available: `https://www.montena.com/fileadmin/technology_tests/documents/technical_notes/TN06B_TEM_stripline_height_versus_frequency.pdf`, Accessed on: Dec 1, 2020.
[21] *Gtem cells emissions and immunity testing in a single, shielded environment*, Lutherbach, Switzerland: Teseq, 2016. [Online]. Available: `https://www.teseq.com/products/downloads/brochure/GTEM_Cells.pdf`, Accessed on: Nov 26, 2020.
[22] F. J. van Dam, "A stripline antenna for radiated immunity testing", Msc thesis, Department of Electrical engineering, Mathematics and computer science, University of Twente, Enschede, The Netherlands, 2011.
[23] *Guide for the selection of the installation size* , Switzerland: Montena, n.d. [Online]. Available: `https://www.montena.com/fileadmin/technology_tests/documents/technical_notes/TN24_RS105_test_installation_size.pdf`, Accessed on: Dec 1, 2020.

DEPARTMENT OF ELECTRICAL ENGINEERING
DIVISION OF ELECTRIC POWER ENGINEERING
CHALMERS UNIVERSITY OF TECHNOLOGY
Gothenburg, Sweden 2021
www.chalmers.se